2019

Imaging through Glass-air Anderson Localizing Optical Fiber

Jian Zhao
University of Central Florida

IMAGING THROUGH GLASS-AIR ANDERSON LOCALIZING OPTICAL FIBER

by

JIAN ZHAO

B.Sc., Sun Yat-sen University, China, 2012
M.S., University of Central Florida, USA, 2014

A dissertation submitted in partial fulfillment of the requirements
for the degree of Doctor of Philosophy
in CREOL/The College of Optics & Photonics
at the University of Central Florida
Orlando, Florida

Summer Term
2019

Major Professor: Axel Schülzgen

ABSTRACT

The fiber-optic imaging system enables imaging deeply into hollow tissue tracts or organs of biological objects in a minimally invasive way, which are inaccessible to conventional microscopy. It is the key technology to visualize biological objects in biomedical research and clinical applications. The fiber-optic imaging system should be able to deliver a high-quality image to resolve the details of cell morphology *in vivo* and in real time with a miniaturized imaging unit. It also has to be insensitive to environmental perturbations, such as mechanical bending or temperature variations. Besides, both coherent and incoherent light sources should be compatible with the imaging system. It is extremely challenging for current technologies to address all these issues simultaneously. The limitation mainly lies in the deficient stability and imaging capability of fiber-optic devices and the limited image reconstruction capability of algorithms. To address these limitations, we first develop the randomly disordered glass-air optical fiber featuring a high air-filling fraction (~28.5 %) and low loss (~1 dB per meter) at visible wavelengths. Due to the transverse Anderson localization effect, the randomly disordered structure can support thousands of modes, most of which demonstrate single-mode properties. By making use of these modes, the randomly disordered optical fiber provides a robust and low-loss imaging system which can transport images with higher quality than the best commercially available imaging fiber. We further demonstrate that deep-learning algorithm can be applied to the randomly disordered optical fiber to overcome the physical limitation of the fiber itself. At the initial stage, a laser-illuminated system is built by integrating a deep convolutional neural network with the randomly disordered optical fiber. Binary sparse objects, such as handwritten numbers and English letters, are collected, transported and reconstructed using this system. It is proved that this first deep-learning-based

fiber imaging system can perform artifact-free, lensless and bending-independent imaging at variable working distances. In real-world applications, the gray-scale biological subjects have much more complicated features. To image biological tissues, we re-design the architecture of the deep convolutional neural network and apply it to a newly designed system using incoherent illumination. The improved fiber imaging system has much higher resolution and faster reconstruction speed. We show that this new system can perform video-rate, artifact-free, lensless cell imaging. The cell imaging process is also remarkably robust with regard to mechanical bending and temperature variations. In addition, this system demonstrates stronger transfer-learning capability than existed deep-learning-based fiber imaging system.

Key Words: fiber imaging, microstructured optical fiber, transverse Anderson localization, deep learning, convolutional neural network.

To my parents, advisor, and friends

ACKNOWLEDGMENTS

During my first few years in CREOL, I had been researching ultrafast optics. Later on, I decided to change my research direction and joined Dr. Axel Schülzgen's group to study micro-structured optical fiber and fiber imaging. It would be impossible to finish my research in a new area and obtain my Ph.D. degree within two and a half years without Axel's help. I would like to express my very great appreciation to Axel. Foremost, I have learned how to do research independently under the guidance of Axel. Axel is very supportive and trustful of my initiatives, and he gives me great freedom to explore new research areas. At the same time, Axel is highly available and offers me expert advice to steer my research in the right direction. I could not imagine having an advisor being better than him.

Besides my advisor, I would like to offer my special thanks to Dr. Shuo Pang and his team members, Zheyuan Zhu and Yangyang Sun who are also my good friends. I collaborate with Dr. Shuo Pang's team closely to turn the deep-learning fiber imaging idea into reality. During this process, they offer me generous help and numerous technical assistance, which also opens a new avenue for my future career.

My sincere thank you goes to Dr. Rodrigo Amezcua Correa and his team member Dr. Jose Enrique Antonio-Lopez. They not only teach me the processing and fabrication technique of microstructured optical fiber but also work with me to investigate how to fabricate a high-quality glass-air Anderson localizing optical fiber. None of my research would have been possible without the technical support from Rodrigo's team.

I would like to thank Dr. Arash Mafi, my external committee member, for his time dedication and helpful discussions related to the glass-air Anderson localizing optical fiber project. We inherit the idea of glass-air Anderson localizing fiber from Arash whose team is the first one to demonstrate endoscopic image transport through polymer Anderson localizing optical fiber. Arash's expertise and theoretical knowledge of the Anderson localizing optical fiber contribute significantly to my research project.

I would also like to thank Dr. Peter J. Delfyett who is also my committee member. While not directly being involved in my final fiber imaging research, Peter has a positive influence on me when I was studying ultrafast optics in CREOL. Peter has been my course teacher, and his ultrafast photonics class led me into this fantastic area for the first time. His passion for research inspires me to explore new horizons.

I would also like to thank my friends, my colleagues from CREOL and the University of New Mexico, past and present group members from the fiber optics lab, for all the good times they brought to me, for all the support from them. Many thanks to Lisi Ouyang, Yuliang Zhang, Xuan Chen, Jia Xu, Qitian Ru, Honglei Yang, Peng Zhao, Yanchun Yin, Jie Li, Wenxu Zhang, Qi Zhang, Shengli Fan, Hongbo Zhu, Seth Smith-Dryden, Rachel Franzetta, Ali Kazemi Jahromi, Behnam Abaie, Mosfata Peysokhan, Juan Carlos Alvarado Zacarias, Amy Van Newkirk, Catia Bernabini, James Anderson, Stefan Gausmann, and Xiaowen Hu.

Last but not least, I would like to express all my gratitude to my family: my mum Xianglan Li, my dad Chuanzeng Zhao and my sister Yunkang Li. Even if my family lives in a small city in China, which is ten thousand miles away from Orlando, they always try their best to support me

both financially and spiritually in the past years. My family continuously motivates me to overcome all the difficulties and go through a hard time. I would not be able to survive without my family.

TABLE OF CONTENTS

LIST OF FIGURES

LIST OF TABLES

LIST OF ABBREVIATIONS

CCD	Charge-coupled Device
C-DCNN	Cell Imaging DCNN
DCNN	Deep Convolutional Neural Network
DMD	Digital Micromirror Device
FOIS	Fiber-optic Imaging System
GALOF	Glass-air Anderson Localizing Optical Fiber
ID	Inner Diameter
MAE	Mean Absolute Error
MCF	Multicore Optical Fibers
MMF	Multimode Optical Fiber
MNIST	Modified National Institute of Standards and Technology
MSE	Mean Squared Error
MSSIM	Mean Structural Similarity Index
NA	Numerical Aperture
OD	Outer Diameter
pALOF	Polymer Anderson Localizing Optical Fiber
SEM	Scanning Electron Microscope
SLM	Spatial Light Modulator
SMF	Single-mode Optical Fiber
SSIM	Structural Similarity Index
TAL	Transverse Anderson Localization

2D	Two Dimensional
TM	Transmission Matrix

CHAPTER ONE: INTRODUCTION

Anderson localization describes the absence of diffusive wave transport in highly disordered medium and was first introduced by Anderson in the context of electron motion [1]. In Anderson's picture, the interference of electron waves experiencing multiple scattering by random defects in the potential landscape results in electronic states localized in space. Since Anderson localization is a consequence of the wave nature of electrons, this concept can also be applied to classical wave systems, including acoustics, elastics, electromagnetics, and optics [2-5]. Among all classical wave systems, the localization of light has attracted lots of attention and related progresses have demonstrated its great potential in device-level applications [6-15]. However, it is difficult to observe the localization of light in three-dimensional systems due to limitation set by the Ioffe-Regel criterion [16]. This criterion states the following: in order for localization to occur, the scattering must be strong enough so that $kl^* \sim 1$, where k is the effective wavevector in the medium and l^* is the mean free path. But this condition is considerably relaxed in 2D systems [17, 18]. Optical waves can be localized in 2D disordered systems, and the localization length ξ, which is the effective beam width in transverse plane, is given by $\xi = l^* exp(\pi k_\perp l^*/2)$ where the mean free path l^* relates to the refractive-index fluctuations and $k_\perp$ is the transverse component of the wavevector k. In a quasi-2D system where the randomness is only limited to the transverse plane, the transverse wavevector component $k_\perp$ can be 10-100 times smaller than k. Therefore, even if the mean free path is much larger than wavelength, localization can still occur [18, 19].

TAL was first proposed numerically by Abdullaev *et al.* and De Raedt *et al.* [17, 20]. In particular, the refractive index in the disordered system introduced by De Raedt *et al.* is distributed randomly in the transverse plane and invariantly along the longitudinal direction. The optical beam

propagating along the longitudinal direction of such a system can maintain a finite beam cross-section due to the TAL in the transverse plane, which resembles the beam propagation in waveguide devices. It has also been found that the localization length depends on the refractive index contrast and the materials filling fraction [17]. The first experimental observation of TAL of light in a similar system was demonstrated by Segev's team in 2007 [18]. In this pioneering work, they use a probe beam to investigate TAL in a photorefractive crystal. The refractive index profile of this crystal is randomly distributed in the transverse plane and invariant longitudinally. However, the small photoinduced refractive index variations ($\sim 10^{-4}$) result in rather large localization beam radii with a large standard deviation among different realizations of the random refractive index profile. Although the TAL beam radius is meaningful in a statistically averaging sense, the self-averaging behavior can guarantee similar levels of localization for different realizations of random profiles if large refractive index variations are introduced to produce strong wave localization [19, 21-24]. In this case, one realization of the statistically identical ensemble of TAL waveguides is practically equivalent to the ensemble average. Therefore, large refractive index variations are desired for pushing TAL optical waveguides to real applications.

The first TAL disordered waveguide with large refractive index fluctuations (~0.1) was developed by Mafi's team in 2012 [19]. This TAL device is a disordered pALOF fabricated by randomly mixing 40000 pieces of polymethyl methacrylate fibers and 40000 pieces of polystyrene fibers. The localized beam radius of pALOF is sufficiently small and comparable to a typical index-guiding optical fiber. Moreover, the large index contrast inside pALOF reduces the sample-to-sample variations of localized beam radii to a level that can satisfy image transmission requirements. Besides large refractive index fluctuations, Karbasi *et al.* further found through a

numerically study that ~50% materials filling fraction is desirable for generating small localized beam radii [21, 23]. Based on a one-dimensional waveguide model, it is also numerically confirmed that the optimal feature size might be around twice the wavelength of operation, and the quality of image transport can be improved in disordered waveguides compared to periodic waveguide structures [23, 25]. In 2014, image transport through pALOF was first experimentally demonstrated and the transported image quality was proved to be comparable to or better than some of the best commercially available multicore imaging fibers [7]. However, the strong signal attenuation in pALOF limits the image transport distance to a few centimeters, too short for most practical applications. Moreover, to further reduce the radius and the sample-to-sample variations of the localized beam the low refractive index contrast is still a bottleneck for pALOF. Recent research on the mode properties of disordered optical fiber unveils that most of the guided modes in pALOF demonstrate single-mode properties [26, 27]. Schirmacher *et al.* further uncover that TAL modes exhibit very unusual wavelength-independent properties [28]. As demonstrated in their work, when tuning the wavelength from ~500 nm to ~1000 nm the localization length of TAL modes remains almost unchanged. This unique property can enable imaging using a broadband light source.

To address the shortcomings of pALOF, the next generation of disordered optical fibers should be made from a glass matrix with randomly distributed air holes across the transverse plane [7, 29]. As proposed by the earlier work, the filling fraction should be around 50% and the optimal average size of the air holes might be twice the operating wavelength. The large refractive index difference (~0.5) between glass and air can further reduce the radii and sample-to-sample variations of the localized optical modes. In addition, the low optical attenuation in glass materials

can extend the imaging transmission distance significantly. The first glass-air based disordered fiber was reported by Karbasi *et al.* in 2012 [30]. It is fabricated from a porous artisan glass with an average air-filling fraction of ~5%. The size of air holes varies from 0.2 μm to 5.5 μm. Due to the low air-filling fraction and non-uniform distribution of air holes, the TAL can only be observed near the boundary of this fiber. To fabricate a glass-air disordered optical fiber with high air-filling fraction and more uniform air-hole distribution, we developed a new fabrication recipe based on the stack-and-draw method and demonstrated a low-loss GALOF with an air-filling fraction of ~28% and an average air-hole diameter of ~1.6 μm [12, 31]. Using this fiber, we report bending-independent image transport through a meter-long GALOF sample and demonstrate that the quality of images transported through the GALOF is comparable to or even better than that transported through commercial multicore fiber for the first time [12]. Fig. 1 shows the SEM image of a typical GALOF sample's cross-section. Our very recent research on the modal properties of GALOF indicates a very high-density (~ 16 modes per μm^2 at ~600 nm) of localized modes with nearly diffraction-limited beam quality and high spatial coherence distributed across the random transverse fiber structure. This is another unique property which is crucial for the achieved high-performance imaging [27]. Overall, the GALOF demonstrates superior imaging capability. More importantly, it lays the foundation for a new generation FOIS.

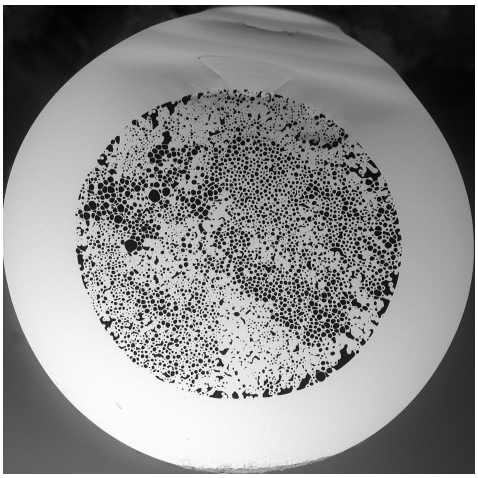

Figure 1.SEM cross-section image of GALOF. The OD is 414 μm, and the diameter of the random structure region is 278 μm with an air-filling fraction of about 28.5%.

Fig. 2 shows a specific type of FOISs, the schematic of a conventional fiberscope. Currently, FOIS plays a critical role in neuroscience and clinical applications [32-35]. In these areas, visualizations of real-time cell activity, morphology, and overall tissue architecture are crucial for fundamental research and medical diagnosis. It usually requires real-time *in vivo* imaging to be performed in a minimally invasive way with the ability to deeply penetrate into organs. Due to the miniature size and flexible imaging transfer capability, FOISs have been widely applied to this domain [32, 34-42]. Current solutions are faced with challenges regarding bulky and complex distal optics, imaging artifacts and extreme sensitivity to perturbations. These limitations mainly originate from the optical fiber device and imaging processing method. For example, MCFs and MMFs are the two most widely used fibers in these systems. Most conventional MCF-based systems usually require extra distal optics or mechanical actuators which limit the extent of miniaturization and induce large penetration damage [32, 33, 41]. The particular core patterns featured in MCFs result in pixelated artifacts in transported images in such system [34, 43-46]. Even if recently reported MCF-based system using wavefront-shaping method can

relieve the pixelated artifacts, the strong core-to-core coupling in MCFs is inherently sensitive to tiny deformation which makes it intolerant to perturbations [47-50]. In addition, the strong crosstalk in MCFs also limits its light source to narrowband illumination and a low mode density [44]. Typical systems using MMF mainly rely on image reconstruction processes using the TM method to compensate for randomized phases through wavefront shaping [35, 38, 39, 51, 52]. While the multimode inference effects inside the MMFs are inherently extremely sensitive to any refractive index changes, even minor changes of temperature (a few degrees Celsius) or slight fiber movement (a few hundred micrometers) can induce mode coupling and scramble the pre-calibrated transmission matrix [35]. In particular, for MMF-based systems, the coherence length of light source needs to exceed the difference between the maximal and minimal optical propagation distance in MMF as indicated in [38]. Therefore, any increase in bandwidth of the light source would decrease the maximum working length of the MMF. For example, as estimated in [38], only ~1 cm of MMF can be used even for a coherent femtosecond laser source with a bandwidth of ~2 THz. In addition, both MCFs and MMFs suffer from low mode densities. For example, the mode densities at ~600 nm wavelength of commercial MMF, and MCF are ~ 1 mode per μm^2, and 0.1 mode per μm^2, respectively. Above-mentioned challenges mainly come from the optical fiber. Regarding the imaging process method, the TM approach is the main solution to perform imaging with MMFs and enhance imaging quality for MCF-based system for most advanced FOISs. Here, the interferometric method and wavefront modulation using SLMs or DMDs are applied to measure the system's TM [53-56]. After knowing the TM of the fiber system, the distorted image can be recovered, and the image quality can be enhanced through wavefront compensation again using SLMs or DMDs. Several shortcomings are raised by this approach. First, regardless of the

type of optical fiber used in FOISs, advanced FOIS that is based on a TM approach is incompatible with broadband incoherent light illumination. Second, the interferometric system for TM measurement makes a sophisticated experimental procedure, complicated and unstable noisy system. Polarization control is also required for TM approach, which makes the bulky interferometric system even more complex. Third, the slow refresh rate of the expensive wavefront-shaping device (SLMs or DMDs) limits the imaging acquisition speed (<10Hz for most systems) and increase the cost (~30k $). Finally, there exist evident artifacts in reconstructed images using the TM approach.

The GALOF is compatible with broadband illumination, has a much higher mode density and demonstrate single-mode like properties. It can overcome the limitations of MCFs and MMFs. However, to fully satisfy those demanding requirements of practical FOISs, GALOF-based systems still face several challenges if merely based on conventional imaging process method similar to the schematic shown in Fig. 2. First, the structure parameters of GALOFs currently limited by the fabrication process need to be optimized for maximum image quality and resolution. Second, a technique has to be developed that allows for imaging of objects at various distances from the transmission fiber facet. Such a variable working distance should be achieved without requiring distal mechanical scanning heads or other distal bulk optical elements that counteract the minimally invasive character of the fiber optic probe. Third, the new method should be able to realize high-quality real-time imaging and avoid complicating the configuration.

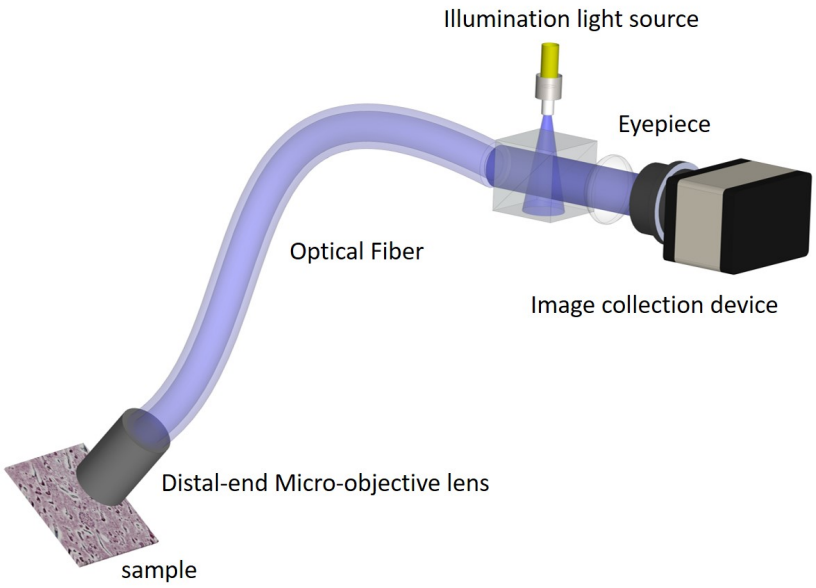

Figure 2. Schematic of a conventional fiberscope. The image of the sample is relayed to the distal end of the optical fiber by a micro-objective lens. The eyepiece at the proximal fiber end images the output facet onto the image collection device. To illuminate the sample, the illumination beam is transmitted using a separate light guide channel.

Thanks to the recently burgeoning deep learning technology [57], it is possible to address these challenges and create a fully flexible and lensless FOISs that delivers artifact-free, high-quality images by combining GALOFs with DCNNs. The DCNN is a data-driven deep-learning technique, which has gained great success in solving imaging problems recently and demonstrated better performance than conventional model-based methods [15, 58-64]. The superior performance of DCNNs roots in that they are the generalization of other possible algorithms [65]. Relying on large-data based training process, the DCNN can learn the physical process of the image transmission through the entire optical system without knowing any models or priors. It particularly fits for the inverse imaging problem of FOISs: the trained DCNN is a precise approximation of the mapping function between the measured imaging data and the input imaging data; well designed and trained DCNNs can be used to predict input images even if the particular

type of images is not included in the set of training data. For example, to describe the image reconstruction process, we could assume that the object intensity image I_{obj}, and the fiber-transported raw intensity image I_{raw} are related by $I_{raw}=HI_{obj}$, where H denotes the forward operator connecting the input object image and the measured raw image. To reconstruct the object I_{rec}, one way is to solve an optimization problem of the form:

$$\tilde{I}_{rec} = \arg min_{I_{rec}} \|HI_{rec} - I_{raw}\|^2 + \gamma\varphi(I_{rec}) \quad (1)$$

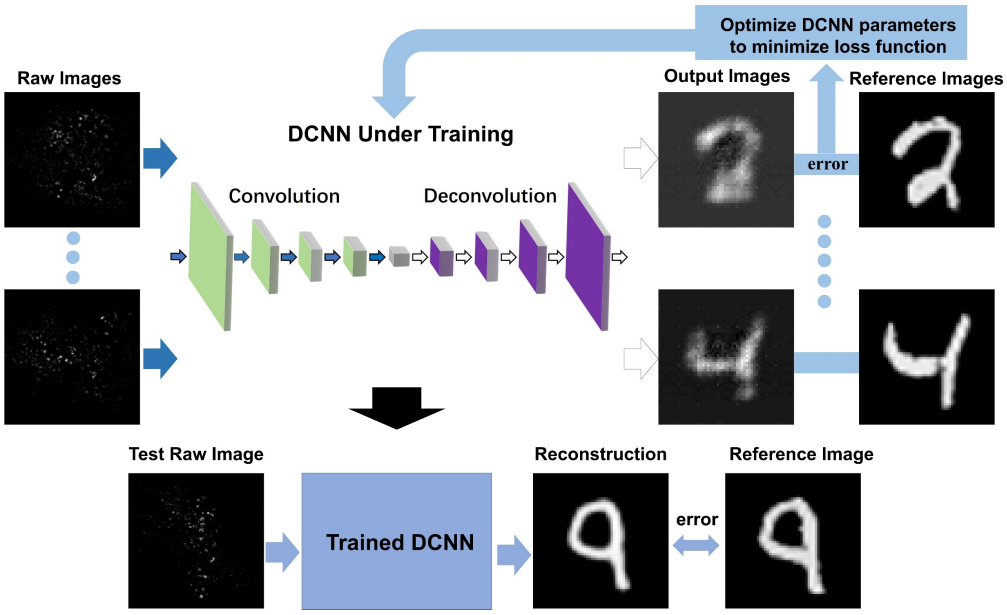

Figure 3. Schematic of the training and reconstruction process using a DCNN.

Where φ is the regularizer encoding the prior knowledge of the object, and γ is the regularization parameter that adjusts the relative strength of the two terms in the optimization process [66, 67]. The problem of this method is that it requires precise knowledge of H and proper selection of φ. For the transmission through the Anderon localizing optical fiber, it is very difficult to develop an accurate physics model of this type, and the simulation process requires huge

computational power [21]. DCNN demonstrates its superiority since it does not require prior knowledge and just needs the computational power of a personal computer for this work. The prediction process is fast and usually takes time on the order of several milli-seconds on regular GPUs. In addition, the DCNN is currently the optimal choice to truly realize lensless imaging since it can accurately simulate the light propagation through the complete system, from the objects to the final CCD detector. Based on this capability, a DCNN can basically replace any distal optics and other image correction or reconstruction tools. Furthermore, the DCNN could remove the drawbacks of the model-based conventional method. For example, most state-of-the-art FOISs heavily rely on wavefront-shaping TM approach which limits these systems to slow imaging speed and narrow bandwidth coherent light source only [50, 55]. In the experiment, the measurement technique of TM is interferometry which results in a complicated, polarization-sensitive and noisy system [50, 53, 54]. In contrast to that, based on DCNNs the TM of the system can be measured just using intensity images from regular CCDs, and no requirements are imposed on the coherence or polarization states of the light source

To illustrate the principle of DCNN-based imaging, the schematic of the DCNN training and image reconstruction process is shown in Fig. 3. Our DCNN applies a deep encoder-decoder architecture [68]. As shown in Fig. 3, the basic idea of a deep encoder-decoder network is to use convolutional operations to extract image features from input raw images first. This process preserves the primary components of input images and eliminates images' corruptions. After going through all convolutional layers to extract the high-dimensional features, corrupted raw images are converted into a "clean" one while subtle details of images may be lost. Following with the convolutional operations, the deconvolutional operation combines the features and recover the

details of images. The final output deconvolutional layer is a recovered original image. To put this DCNN model into practice, it needs to be trained first. The training process generates a computational architecture that accurately maps the images transported by the optical fiber to its original objects. Training of the DCNN requires a large number of matched input (reference images of original objects) and output (the transported raw images) pairs to optimize the parameters of the neural network and build a suitable computational architecture. Refer to Fig. 3, in the training phase (with randomly initialized parameters) raw images are sent into the DCNN to obtain output images. The loss function is required to measure the difference between output images and the reference images. A higher error value of loss function indicates the prediction of the DCNN deviates from the correct direction. If the output of the DCNN matches with reference images well, the loss function should output a low error value. The DCNN is trained through an iterative optimization process by minimizing the loss function between the output images and their corresponding reference images. Specifically speaking, the MAE metric is applied as a loss function in our work to compare the reconstructed images with the corresponding reference images. The MAE is defined as $\left|\tilde{I}_{rec} - I_{obj}\right|/(wh)$, where w and h are the width and height of the image. The optimizer needs to work with the MAE loss function to minimize the error through tuning the parameters of the DCNN. The specific mathematical method to update the parameters are the optimizer. The loss function tells the optimizer the right direction in the training process. In our model, we apply the Adam optimizer since it is a frequently used and very effective optimizer [69]. After the training, the parameters of the DCNN are fixed, then the DCNN is applied to reconstruct images from the raw images of a separate test set. The reconstruction time per test image is usually on the order of a few milliseconds with a personal computer and regular GPUs. In addition, a

separate set of image pairs serves as a test set to evaluate the performance of the trained DCNN. In this test process, the MAE is also applied as the metric.

In the following chapter, we discuss our recent progress in the development of GALOF and GALOF-based imaging systems. In **Chapter two**, the fabrication process, structure parameters and imaging capabilities of GALOF are shown. We also demonstrate recent research on the beam quality of highly-localized modes in GALOF.

In **Chapter three**, recent research on the beam quality of highly-localized modes in GALOF is discussed.

Chapter four presents basic principles and novel experimental results of the first DCNN/GALOF FOIS. This imaging system works with coherent illumination and performs simple imaging task with sparse binary objects.

In **Chapter five**, we show the latest DCNN/GALOF system which realizes real-time robust cell imaging under incoherent broadband illumination.

CHAPTER TWO: IMAGE TRANSPORT THROUGH GALOF

2.1 Experimental Procedure and Imaging Quality Evaluation Metrics

The SEM image in Fig. 1 shows a typical GALOF cross-section. The outer diameter of this GALOF is ~ 414 μm and the diameter of the disordered structure is ~ 278 μm with an air-filling fraction of ~28.5%. GALOFs are fabricated at CREOL using the stack-and-drawn method [12, 15]. Thousands of silica capillary tubes are fabricated with different ODs as well as different ratios of ID to OD. The OD of the silica capillaries ranges from ~100 μm to ~180 μm, and the ID/OD ranges from 0.5 to 0.8. The capillaries are mixed randomly and fed into a jacket to make the perform. Once the preform is completed, it is drawn to canes with around 3 mm outer diameter. Subsequently, the cane is drawn to the desired fiber size. Fig. 4 shows three different GALOF samples which have different maxima in the air-hole-area distributions but similar air-filling fractions. The air hole area distributions of GALOF(1), GALOF(2), and GALOF(3) in Fig. 4 have maxima of 2.5 μm^2, 6.8 μm^2, and 18.5 μm^2, respectively. With a similar air-filling fraction, the localization length depends on the feature size of air holes.

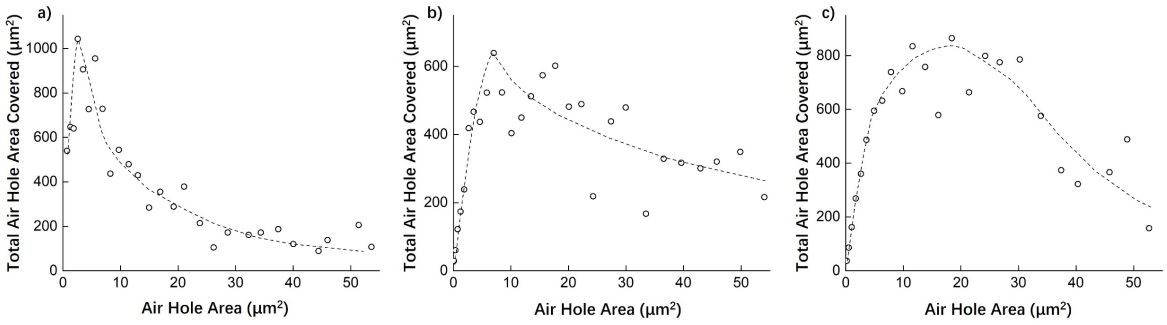

Figure 4. Statistical distributions of air-hole areas in the GALOF samples. a) is GALOF(1); b) is GALOF(2); c) is GALOF(3).

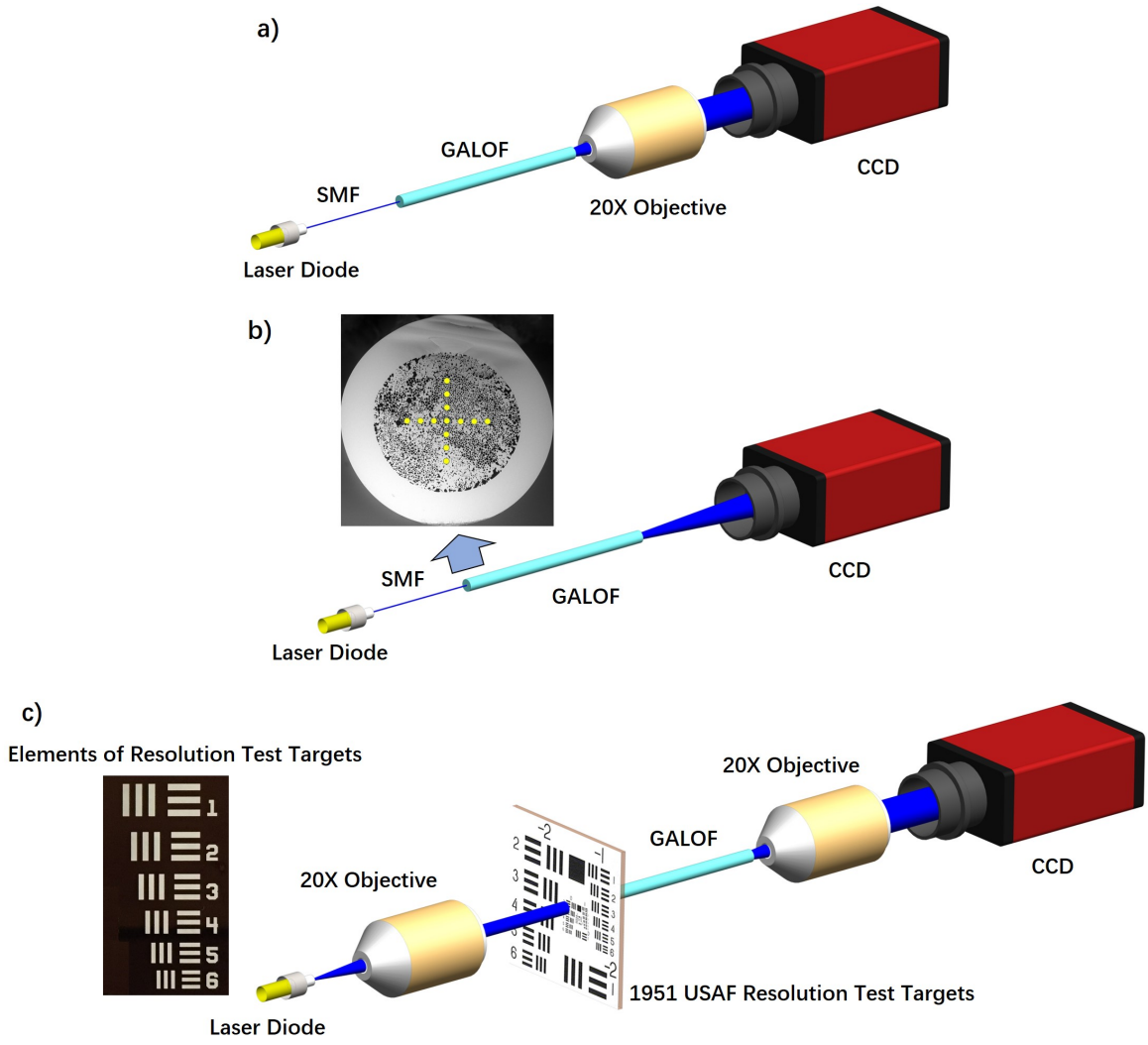

Figure 5. Experimental configurations for localization lengths measurement, NA measurement, and image transport. a) Setup for measuring localization lengths. The laser beam from a laser diode is coupled into an SMF. The SMF is butt-coupled into the input facet of the GALOF sample. The output facet of the GALOF sample is imaged onto a CCD camera. b) Setup for NA measurement. The configuration is similar to a) except that the objective is removed. An SMF is butt-coupled into the GALOF input facet to deliver a laser beam with a wavelength of 405 nm. For each coupling position, the far-field beam profile is recorded by a CCD camera. As shown by yellow dots in the disordered region, there are 13 different coupling locations in the cross-section of the GALOF. The distance between the neighboring position is 25 μm. c) Setup for image transport through the GALOF. The elements in a 1951 USAF resolution test target (Thorlabs R3L3S1N) work as the objects. Various elements of the resolution test target are illuminated by a collimated beam from a CW laser beam. The image of illuminated elements in the resolution test target is coupled into the random structure of the GALOF sample, and the output facet of the fiber is imaged onto a CCD camera using a 20X objective.

In analogy to reference [19], we measure the localization length of GALOF(1), GALOF(2) and GALOF(3) with air-hole area distributions as shown in Fig. 4 using the setup in Fig. 5 a). Lengths of measured three samples are 4.5 cm. A 635 nm CW laser is used as the light source. We locate the SMF at 13 different (x,y)-input positions of the disordered structure in the GALOF samples, and record 13 output beam profiles by a CCD camera (Gentec-EO Beamage-3.0) for each GALOF sample. For each recorded beam profile, the localization length can be estimated based on the inverse participation ratio defined by the following formula [70]:

$$L^2 = \frac{[\iint I(x,y)dxdy]^2}{\iint I(x,y)^2 dxdy} \tag{2}$$

where L is the localization length, and $I(x,y)$ is the beam intensity at position (x,y). Then we obtain an estimate for the localization length of each GALOF sample by averaging the 13 calculated values. The inverse participation ratio is originally rooted in the definition of the mode effective area in nonlinear optics. To better represent the Anderson localization phenomena and the random-walk nature of the scattered wave, the statistical second-moment method might be a preferable [29]. The localization length can be calculated using this method as [29]:

$$L^2 = \iint E(x,y)|(R-\bar{R})^2|E(x,y)dxdy \tag{3}$$

$E(x,y)$ is the optical field and assumed to be normalized according to $\iint E(x,y)E(x,y)dxdy = 0.5$. R is the transverse position vector, and $\bar{R}$ is the vector pointing to the center of the beam, defined as the mean intensity position by $\bar{R} = \iint E(x,y)RE(x,y)dxdy$. Since the localized beams in our experiments are mainly single-lobed, formula (2) and (3) would give similar results. We adopt formula (2) to calculate the localization length.

NA is another important parameter related to the imaging capability of the GALOF. In order to quantify the NA of the GALOF sample, we build up the setup shown in Fig. 5 b). We scan 13 different coupling locations in the disordered region and measure corresponding far-field emission angles at the output end of the fiber. The NA can be estimated from these far-field angles.

To investigate the imaging capability of the GALOF, we use the experimental setup shown in Fig. 5 c). The GALOF(1) sample is applied in all related experiments. To make a comparison, a commercial fiber bundle sample (FIGH-10-500N) is installed in the same setup to perform image transmission. A 1951 USAF resolution test target is placed directly in front of the cleaved input facet of the fiber under investigation. Both the GALOF and the commercial imaging fiber are cleaved with a large diameter fiber cleaver (Vytran LDC-400). Various elements of the resolution target are illuminated by a collimated beam from a CW laser diode with a wavelength of 405 nm or 635 nm. The light transmitted through the resolution test target is coupled into the disordered fiber region, and the output facet of the fiber is imaged onto a CCD camera (Gentec-EO Beamage-3.0) using a 20X objective. Transported images have been collected for three different cases: 1) Images are transmitted through 4.5 cm of a straight GALOF(1) sample and a straight commercial fiber sample; 2) Images are transported through 90 cm of a straight GALOF(1); 3) Images are transported through a 90 cm GALOF(1) segment that has a bend to form an 180 degree turn with a bend radius of 20 cm. All these experiments are repeated for different wavelengths. We also performed a separate experiment to transport and collect images going through 4.5 cm of straight GALOF(1), GALOF(2) and GALOF(3) with the purpose of investigating the impact of the feature size on image quality.

To quantify the imaging quality, two widely used metrics, MSE and MSSIM are introduced in our analysis. Higher MSE or lower MSSIM values indicate decreased imaging quality. MSE is defined as follow [71] :

$$MSE = \frac{1}{M \times N} \sum_{i=1}^{N} \sum_{j=1}^{M} (X_{i,j} - Y_{i,j})^2 \quad (4)$$

where X and Y are two 2D matrices that contain pixel intensities of distorted and reference images, respectively. M and N stand for the size of the matrices. MSSIM is calculated by averaging the SSIM [71, 72]. The SSIM is applied to compare the local image patches between the distorted image X and the reference image Y. It is defined as follow:

$$SSIM(X, Y) = \frac{(2\mu_X\mu_Y + C_1)(2\sigma_{XY} + C_2)}{(\mu_X^2 + \mu_Y^2 + C_1)(\sigma_X^2 + \sigma_Y^2 + C_2)} \quad (5)$$

μ_X and μ_Y are the local mean intensities of X and Y. σ_X and σ_Y are the local standard deviations of image X and Y. σ_{XY} is the cross correlation of X and Y. C_1 and C_2 are defined as $(K_1L)^2$ and $(K_2L)^2$, respectively. L is the dynamic range of the image. K_1 and K_2 are two constants, and K_1, $K_2 << 1$. These constants are used to avoid unstable results and somewhat arbitrary. The SSIM index is not sensitive to the variation of their values. Based on the definition of SSIM, MSSIM is calculated by equation (6) as follow:

$$MSSIM(X, Y) = \frac{1}{M} \sum_{j=1}^{M} SSIM(x_j, y_j) \quad (6)$$

In equation (6), x_j and y_j are the image contents at the j^{th} local window of the distorted image X and reference image Y, respectively. The number of local windows is M.

Both MSE and MSSIM are two widely used and recognized metrics for similarity and signal quality assessment in optics and imaging community. MSE has been the dominant metric to quantitatively assess the imaging quality and fidelity for more than 50 years and is the preferred tools for optimizing image processing algorithms [71]. However, in the reference [71], Z. Wang *et al.* point out the MSE is not sensitive enough when being applied to predict human perception of image fidelity. As suggested by both reference [71] and reference [72], the MSSIM is a second imaging evaluation metric which is very sensitive to negligible loss of human visual imaging quality. Therefore, in order to reach a solid conclusion, we adopt both the MSE and MSSIM to calculate the loss of imaging fidelity.

2.2 Results and Discussions

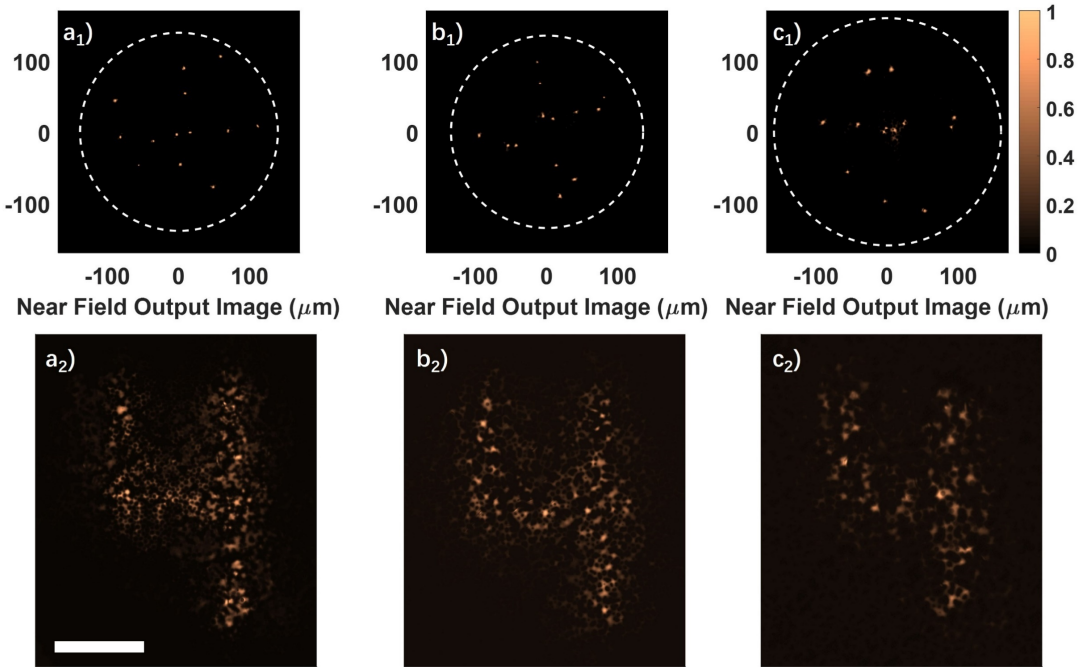

Figure 6. Near field output images for multiple excitation positions and number "4" from group 3 on the resolution test target recorded after transmission through a) GALOF(1), b) GALOF (2), and c) GALOF (3), respectively. The length of the samples is 4.5 cm. The length of the scale bar in a_2) is 50 μm. The MSE values are 0.049, 0.051 and 0.054 for a_2)-c_2), respectively. The MSSIM values are 0.317, 0.263 and 0.241 for a_2)-c_2), respectively.

In Fig. 6 a_1) to c_1) all 13 output beam profiles measured for each GALOF are stacked on top of each other to create one single image per GALOF. The white dashed line circles indicate the boundary of the disordered structures. Then we obtain an estimate for the localization length of each GALOF sample by averaging the 13 calculated values. Based on this method, the approximate localization lengths are 5.2 μm, 5.4 μm, and 6.8 μm for GALOF (1), GALOF (2), and GALOF (3), respectively. The corresponding feature sizes with maximum statistical distributions are about 1.6 μm, 2.6 μm and 4.3 μm for GALOF(1)-GALOF(3), respectively. Therefore, it is experimentally confirmed that the localization length is decreasing with feature

size [12]. To provide a first glance of the effect of varying the air hole distribution, we collected images transported through three GALOF samples with different maxima in the air hole area distributions but similar air filling fractions. These transported images are shown in Figs. 6 a_2)-c_2). The measurements shown in Figs. 6 a_2)-c_2) are obtained using 4.5-cm-long GALOF(1), GALOF(2) and GALOF(3), respectively. The peak airhole areas in the airhole-area distributions of GALOF(1), GALOF(2) and GALOF(3) are 2.5 μm^2, 6.8 μm^2 and 18.5 μm^2, respectively. The calculated MSE and MSSIM values are listed in the caption of Fig. 6. It is clear that an increase in the maximum of the airhole area distribution from 2.5 μm^2 to 6.8 μm^2 and 18.5 μm^2 leads to a slight decrease in the image quality. Although this is not at all a complete exploration of the possible parameter space for image transport in fibers with randomly disordered structures, it is found that there is a general trend of a reduction in transported image quality when the air hole areas are increased within the range of investigation from about 2 μm^2 to 20 μm^2. This also coincides with an observed increase of the localization length for larger air hole areas as shown in Figs. 6 a_1)-c_1). Reasons for this trend include the fact that the mean free path for wave scattering increases with feature size resulting in a larger localization radius, and, therefore, a degradation in image quality and resolution. However, it should be noted that there are other factors influencing the image transport quality and resolution, for example, the air filling fraction and the width of the feature size distribution.

The far-field beam radius versus the recording distance is shown in Fig. 7. For each input coupling position, the CCD is moved far away from the initial position with a step of 2 mm to record 7 far-field beam profiles. The beam radius can be extracted from the beam profile, and far-field emission angles can be calculated from slopes of those lines. This angle varies slightly from position to position indicating that there is not one well-defined NA for GALOFs. However, the

observed average far-field emission angle around 11.5 degree provides at least experimental information that can be used for imaging system design and performance evaluation.

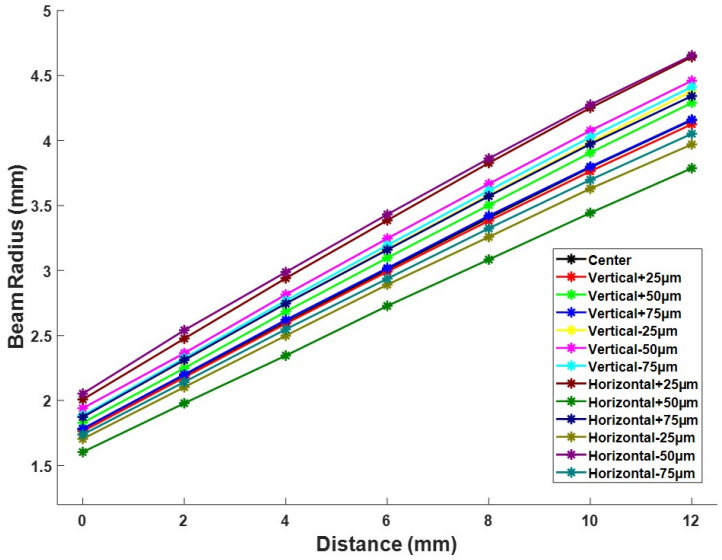

Figure 7. Far-field emission angle measurement results. As the setup shown in Fig. 5 b), the CCD camera records the beam profile at the output end of the GALOF. From the beam profile, the value of the beam radius can be extracted. For each input coupling position, the CCD camera is located at 7 different positions along the beam propagation direction with a step of 2 mm. The measurement is repeated for 13 different input coupling positions.

The smaller localized beam radius in GALOF(1) makes it a preferable candidate for imaging devices. Using the resolution test target and experimental setup shown in Fig. 5 c), the image transport capability and spatial resolution can be evaluated. Figs. 8 a)-c) are images of numbers on the resolution test target transported through a 4.5cm-long GALOF(1) sample. The transmitted images have high visual quality and the same size as the original target elements. To quantify the resolution limit for transportation through GALOF, line elements on the resolution test targets are transported through samples of different lengths. The smallest line elements that can be resolved

are recorded with the CCD camera. As shown in Figs. 8 d) and e), the spatial resolution of a 4.5 cm-long GALOF(1) sample is ~8 μm, while it is ~14 μm for a 90 cm-long GALOF(1) segment. The degradation of resolution for a longer piece of sample is attributed to slight variations along the longitudinal direction due to fabrication imperfections. The resolution of GALOF(1) is comparable to some of the best commercial MCF bundles [12]. GALOFs potentially have several advantages over MCFs. First, there exist more modes in GALOFs than in MCFs. The number of localized modes inside GALOF(1) is on the order of 10^6 [27].The MCF bundle with comparable flexibility and size can only support ~10^4 modes [43, 44]. Although the number of modes in some commercial MCFs can reach 10^5 (Fujikura FIGH-100-1500N), their huge diameters (~1.5 mm) make the fiber bundle non-flexible and entail a high risk for collateral penetration damage in biological objects. Second, the cross-talk between individual cores of MCFs results in a degradation of the point spread function with increasing transmission distance. For example, as demonstrated in [44], the mode coupling in MCFs can transfer optical power to neighboring cores dramatically by just tuning the wavelength within a band of ~7 nm. This kind of mode coupling would seriously impair the imaging process. In GALOFs the point spread function is directly related to the localization length, which is independent of transmission distance [25]. In particular, very recent research further proves that the localization length in TAL fibers is wavelength independent. This enables the implementation of broadband and incoherent imaging using GALOFs. In addition, the cost of GALOFs is potentially lower than the cost of MCFs since GALOFs require only a single material and the fabrication process is straightforward. In contrast, MCFs require expensive highly-doped materials to increase the numerical aperture of the individual cores to suppress the crosstalk [45, 73]. Moreover, it requires multiple stack-and-draw

procedures to fabricate a high-quality MCF bundle [45, 73]. This complicated process is reduced to only two steps for fabricating GALOFs: 1. Draw silica canes from preforms; 2. Draw GALOFs from canes [12]. Overall, the GALOF is the first disordered optical fiber which exhibits all features for practical applications and has the potential for performance superior to conventional MCF imaging bundles.

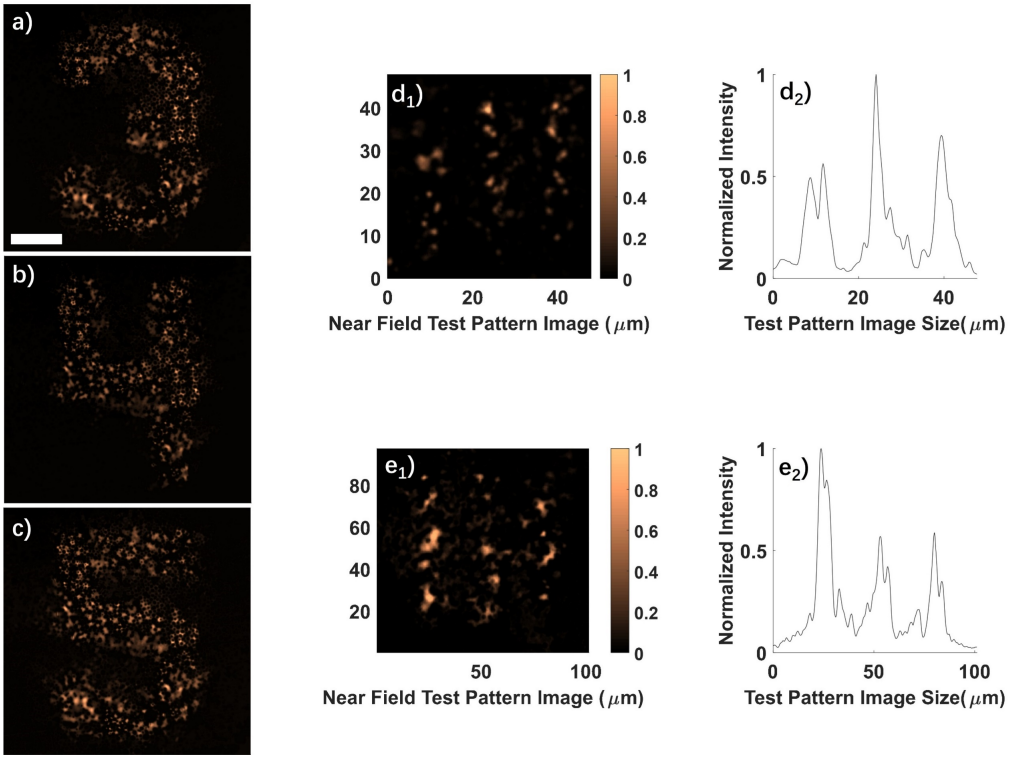

Figure 8. Transported images of different numbers of group 3 on the 1951 USAF test target and spatial resolution characterizations. The length of the scale bar in a) is 40 μm. a)-c) are transported images of different numbers of group 3 on the 1951 resolution test target using a 4.5cm-long sample. d)-e) are images of the smallest resolvable line elements of the resolution test targets and the corresponding intensity profiles of the line elements after transport through a GALOF(1) sample. d_1)-d_2) are obtained from a 4.5cm-long sample. line elements in d_1) belong to group 6 number 1 on the resolution test target with a line width of 7.8 μm; the integrated cross-sections in d_2) are obtained by integration along the line elements. The visibility value $(I_{max} - I_{min})/(I_{max} + I_{min})$ for the data in d_2) is about 0.77. e_1)-e_2) are obtained from a 90cm-long sample. line elements in e_1) come from group 5 number 2 on the resolution test target. The visibility of e_2) is about 0.73

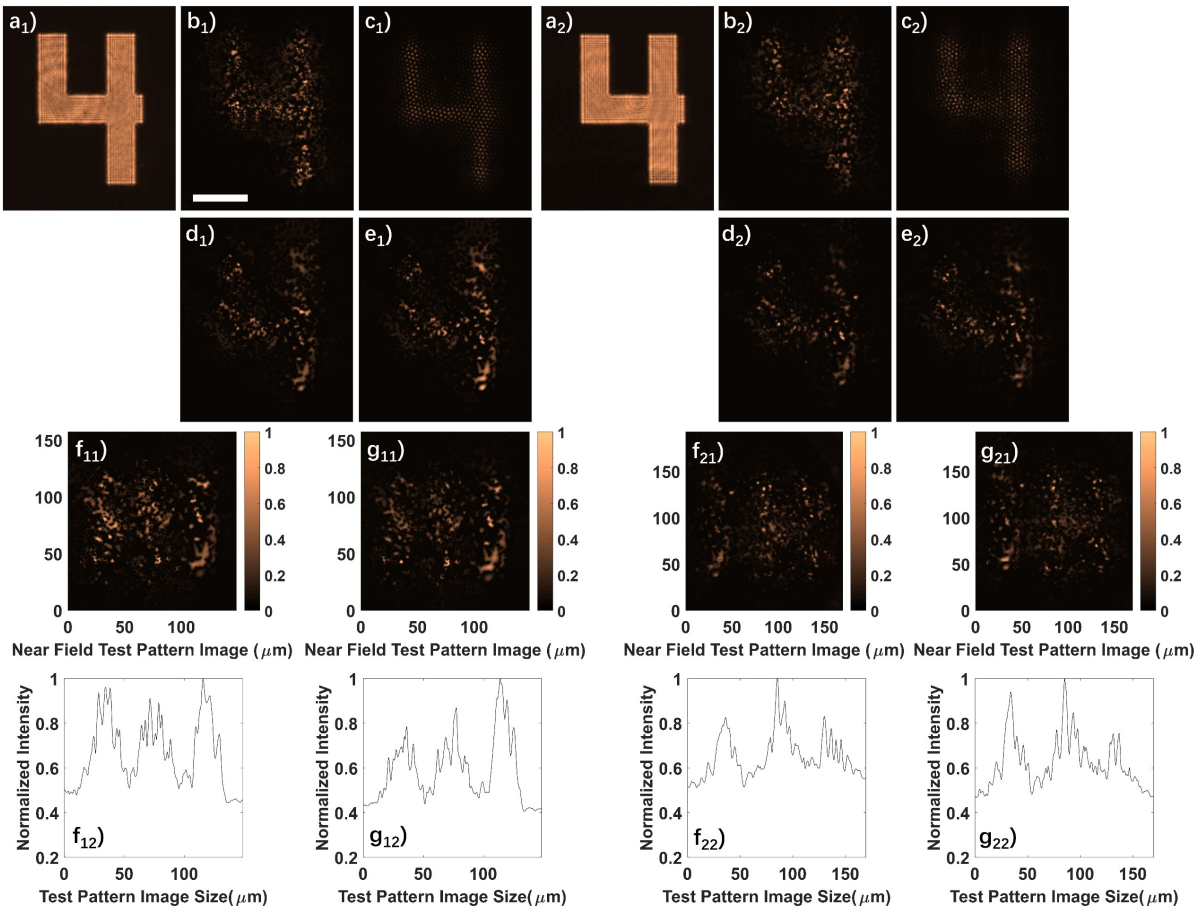

Figure 9. Comparison with the commercial MCF and image transport through meter-long straight and bent GALOF. The reference images a_1) and a_2) are measured without any fiber. b)-e) are images of the digit "4" from group 3 on the 1951 resolution test targets after transport through different fiber samples with different illumination wavelength. The length of the scale bar in b_1) is 50 μm. b)-c) are obtained from 4.5cm-long samples, and d)-e) are obtained from 90cm-long samples. f)-g) are images of line elements and the corresponding intensity profiles of the line elements after transport through 90 cm of GALOF. The line elements in f_{11}) and g_{11}) belong to group 4 number 5 on the resolution test target. The line elements in f_{21}) and g_{21}) belong to group 4 number 3. The visibility values are 0.35 for f_{12}), 0.33 for g_{12}), 0.26 for f_{22}), and 0.31 for g_{22}), respectively. The wavelength for a_1)-g_1) is 405 nm while the wavelength for a_2)-g_2) is 635 nm. c_1) and c_2) are images transported through commercial imaging fiber FIGH-10-500N. b_1), b_2) and d)-g) are images transported through GALOF samples of different lengths. d_1), d_2), f_{11}) and f_{21}) are obtained keeping the GALOF straight, while e_1), e_2), g_{11}) and g_{21}) are obtained using the same sample with a 180-degree turn (20 cm bending radius).

Table 1 MSE and MSSIM values of transported images for 4.5 cm-long fiber sample

	GALOF(1)		FIGH-10-500N	
λ	405 nm	635 nm	405 nm	635 nm
MSE	0.049	0.055	0.053	0.056
MSSIM	0.317	0.252	0.315	0.237

Table 2 MSE and MSSIM values of transported images for 90 cm-long GALOF sample

	Straight		Bent	
λ	405 nm	635 nm	405 nm	635 nm
MSE	0.053	0.060	0.051	0.060
MSSIM	0.246	0.206	0.306	0.215

For a detailed evaluation, the imaging performance of the GALOFs (see Fig. 9) has been analyzed quantitatively and compared with the commercially available Fujikura FIGH-10-500N MCF. The length of all fiber samples used in Figs. 9 b)-c) is 4.5 cm, and the number "4" from group 3 in the resolution target has been transported. The wavelength used in Figs. 9 a_1)-g_1) is 405 nm, while the wavelength used in Fig. 9 a_2)-g_2) is 635 nm. Fig. 9 b_1) and b_2) are image transportation results utilizing the same short GALOF sample; c_1) and c_2) are imaging results of the same FIGH-10-500N sample. The reference images used for the calculation of MSE and MSSIM values are shown in Figs. 9 a_1) and a_2). These images were obtained without any fiber in the imaging set-up. The MSE and MSSIM values of Figs. 9 b)-c) are listed in Table 1 where higher MSE or lower MSSIM values indicate decreased imaging quality. For practical applications that require flexible imaging fiber, the transport of high-quality images through a meter-long fiber, even with tight bends, is a key performance parameter. Images of numbers and line elements that have been transported through the same 90 cm-long straight and bent GALOF are shown in Figs. 9 d)-g). The number "4" also comes from group 3 on the resolution target. Figs. 9 d) and f) are

images through 90 cm of straight GALOF; e) and g) are images through the same 90 cm-long GALOF sample with a 180-degree turn (20 cm bending radius).

Refer to Table 1, comparing the MSE and MSSIM values under the same wavelength the GALOF sample demonstrates better imaging performance than the commercial MCF. Refer to the data in both Table 1 and Table 2, the imaging quality is lowered down when increasing wavelength for the same fiber sample. For the disordered optical fiber, the origin of this wavelength dependence needs to be further investigated. There is no evidence that the imaging quality is directly linked to the localization length. Therefore, it does not conflict with the recent study which demonstrates that the localization length is wavelength independent [28]. For commercial imaging MCF, it is due to the increased core-to-core coupling. Furthermore, the data listed in Table 2 confirm that bending, at least to radii above 20 cm, does not result in a decrease of the quality of the transported images. The bending radius is limited to 20 cm to avoid breaking the GALOF. In addition, images of the smallest resolvable 3-line elements have also been taken to quantify the achievable spatial resolution under the same experimental conditions for 90 cm-long GALOF sample. Figs. 9 f_{11}) and g_{11}) are images of line elements from group 4 number 5 of the resolution target with a line width of 19.69 mm, while Figs. 9 f_{21}) and g_{21}) are images of line elements from group 4 number 3 with a line width of 24.8 mm. Based on these results, we can conclude that image transport through meter-long GALOF is bending-independent for both image quality and spatial resolution, an observation that might be related to the single mode nature of the localized states in disordered fibers [26]. Most importantly, image quality, spatial resolution, and image brightness are only slightly lower when comparing transport through 90 cm and transport through 4.5 cm of GALOF. These small degradations might be attributed to the slight variation of fiber

and feature dimensions along the light propagation direction due to fabrication imperfections. In sum, above quantitative evaluations of transported image qualities confirms that: 1) The imaging quality of GALOF is comparable to some of the best commercial MCFs; 2) The GALOF-based imaging is bending-independent; 3) Shorter wavelengths can improve imaging quality [12]. Particularly, bending-independent imaging makes the GALOF suitable for making a practical optical fiber endoscope where flexibility is extremely important.

CHAPTER THREE: HIGH-QUALITY WAVEFRONT IN GALOF

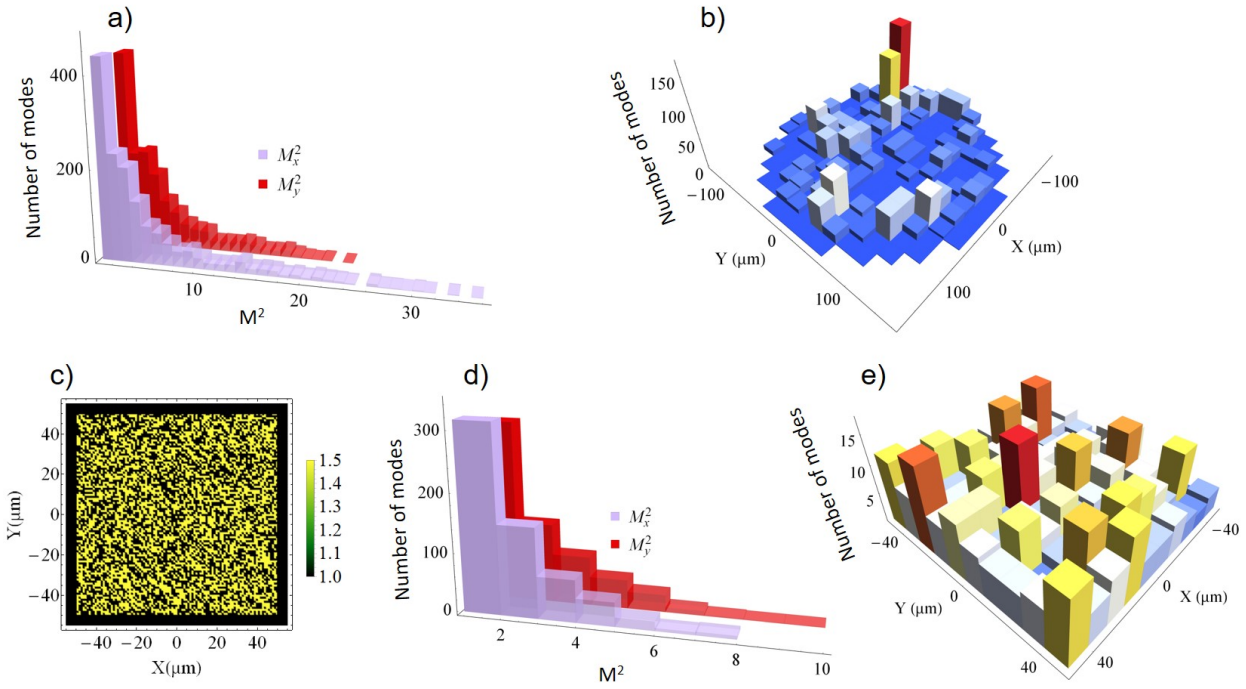

Figure 10. M^2 values and distributions of localized modes in GALOF. a) Histogram of numerically calculated M^2 values for 1500 localized modes in the real GALOF. The vertical axis in a) represents the total number of modes for different M^2 values. b) Density histogram of the positions of the modes in a) within the GALOF cross-section. The value of each pixel in b) corresponds to the number of localized modes. c) Refractive index profile of an optimal-designed GALOF with a 50% air-filling fraction. d) Histogram of numerically calculated M^2 values for nearly 500 localized modes based on c). e) Corresponding density histogram of the mode positions across the profile shown in c).

Recently, we have shown, both numerically and experimentally, that a large number of localized modes in GALOF exhibit high-quality wavefronts and high spatial coherence making these transmission channels comparable to single-mode optical fibers [27]. The GALOF sample used in our work is very similar to the GALOF shown in Fig. 1. We first calculated the localized modes in the GALOF and evaluated their beam quality. For our numerical calculations, we use the finite element method and extract the geometrical GALOF parameters from an SEM image. A

working wavelength of 632.8 nm is chosen to match the wavelength of the He-Ne laser used in the experiment. To obtain the M^2 value for the mode quality analysis, modes are numerically propagated in free space after leaving the GALOF using a fast Fourier transform algorithm. The beam waist in the Cartesian coordinates $x(y)$ is calculated by $w_x = 2\sigma_x$ ($w_y = 2\sigma_y$) where $\sigma_x(\sigma_y)$ is the standard deviation of the mode intensity profile:

$$\sigma_x^2 = \int dA(x - \bar{x})^2 I(x, y) \tag{7}$$

$$\sigma_y^2 = \int dA(y - \bar{y})^2 I(x, y) \tag{8}$$

$$\bar{x} = \int dAxI(x, y) \tag{9}$$

$$\bar{y} = \int dAyI(x, y) \tag{10}$$

where $dA=dxdy$, $(\bar{x}, \bar{y})$ represents the mode center coordinates and $\int dAI(x, y) = 1$. M^2 values (M_x^2, M_y^2) are then obtained using the variance method [27]. An M^2 value of ~1 is strong evidence of nearly diffraction-limited beam quality. The obtained simulation results are shown in Fig. 10.

The results shown in Fig. 10 a) demonstrate that $M^2 < 2$ modes are statistically dominant in the GALOF indicating the presence of abundant localized modes with high-quality wavefronts. The distribution of the corresponding transverse positions within the GALOF cross-section is shown in Fig. 10 b). Relative uniform distribution can be observed while some local hot spots also exist. The existence of those non-uniform areas might be attributed to the non-uniformity of air-hole sizes and air-filling fractions across the GALOF profile. The regions in GALOF with low air-filling fractions can reduce the number of high-quality modes. This observation is further

confirmed by simulation using an optimal-designed refractive index profile shown in Fig. 10 c). The size of unit cells in this cross-section is 1 μm. Air and glass are mixed randomly with an equal probability to reach a uniform 50% air-filling fraction. The histogram of M^2 values for nearly 500 modes and their position distribution across the fiber cross section are shown in Figs. 10 d) and e). Modes with M^2 values smaller than 2 are much more dominant when compared to the real GALOF calculations shown in Fig. 10 a). Simultaneously, the uniformity of modes distribution is also greatly improved. These calculations indicate that uniform distributions of air-hole size and high air-filling fraction enhance the localization strength and the mode quality. The simulations provide guidance for future GALOF developments and are encouraging regarding potential improvements in GALOF performance.

Experimental investigations also support the numerical simulation results [27]. The experimental setup shown in Fig. 11 a) is applied to excite localized modes and evaluate their M^2 values. The measured M^2 value distributions of 30 modes are shown in Fig. 11 b). Most modes exhibit $M^2 < 2$. Besides a low M^2 value, another unique feature related to high-quality wavefronts is a high degree of spatial coherence. To demonstrate the spatial coherence, one localized mode is excited and used to illuminate the double slit inserted in the output beam path, see Fig. 11 c). The far-field interference pattern generated by the mode after passing through the double slit is shown in Fig. 11 d). Fig. 11 e) is the corresponding vertically averaged intensity distribution. High-contrast interference fringes in Figs. 11 d) and e) indicate the high degree of spatial coherence for the localized mode.

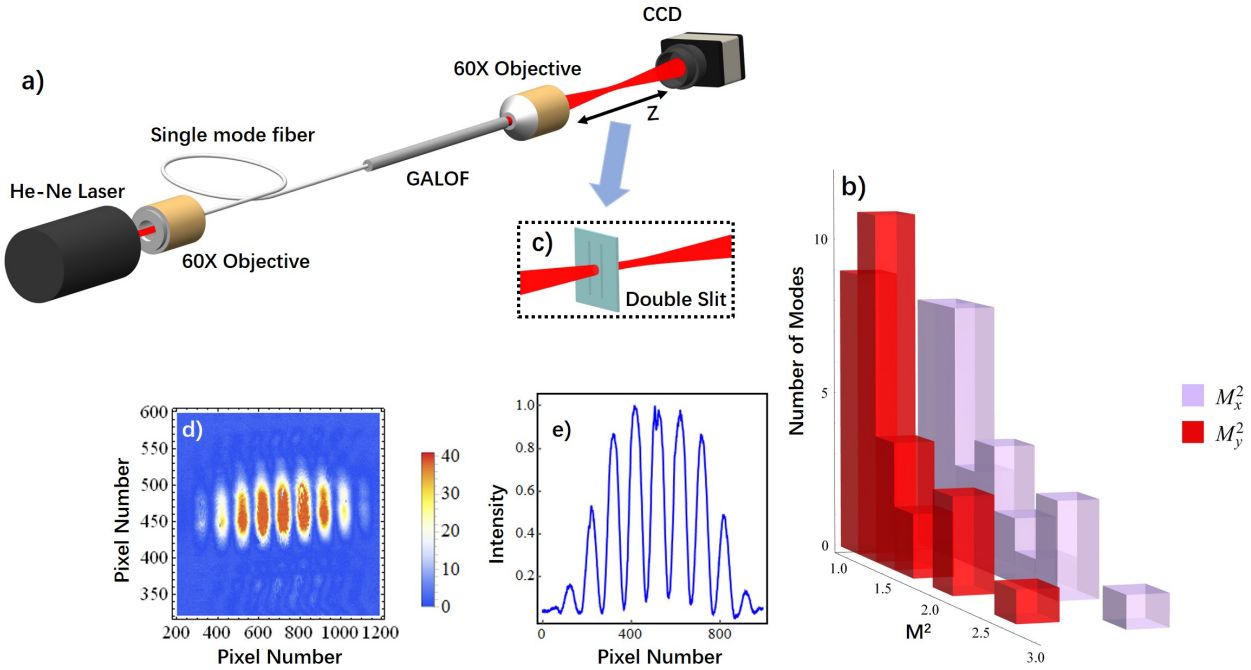

Figure 11. Experimental measurement of M^2 values and characterization of spatial coherence. a) Experimental setup for M^2 measurements. A He-Ne laser beam is coupled into an SMF and butt-coupled to the input facet of a 155-cm long GALOF. The SMF is scanned across the input facet to excite various localized modes. Beam profiles located at different positions along z-axis are recorded by a CCD beam profiler to extract M^2 values. b) Histogram of M^2 values for 30 localized modes measured in the experiment. c) Double slit (slit separation: 500 μm, slit width: 80 μm) inserted in the same setup for spatial coherence evaluation. d) The interference pattern generated by the localized mode. e) Intensity distribution averaged over the vertical direction of the pattern in d).

Due to its large transverse size, the GALOF possesses several thousands of modes. The existence of abundant high-quality localized modes gives rise to the high potential of GALOF for imaging applications. These localized modes can be easily excited without the assistance of complicated and expensive SLM and applied to encode and transport imaging information. The high-quality wavefronts and the large degree spatial coherence of the localized modes result in single-mode-like properties making the GALOF transmission properties remarkably robust with respect to external perturbations. The theoretical analysis indicates that further improvements

regarding mode quality are possible in further optimized GALOFs demonstrating the GALOF potential for next-generation fiber endoscopes.

CHAPTER FOUR: DEEP LEARNING IMAGING THROUGH GALOF

4.1 Deep-learning Experimental Method and DCNNs

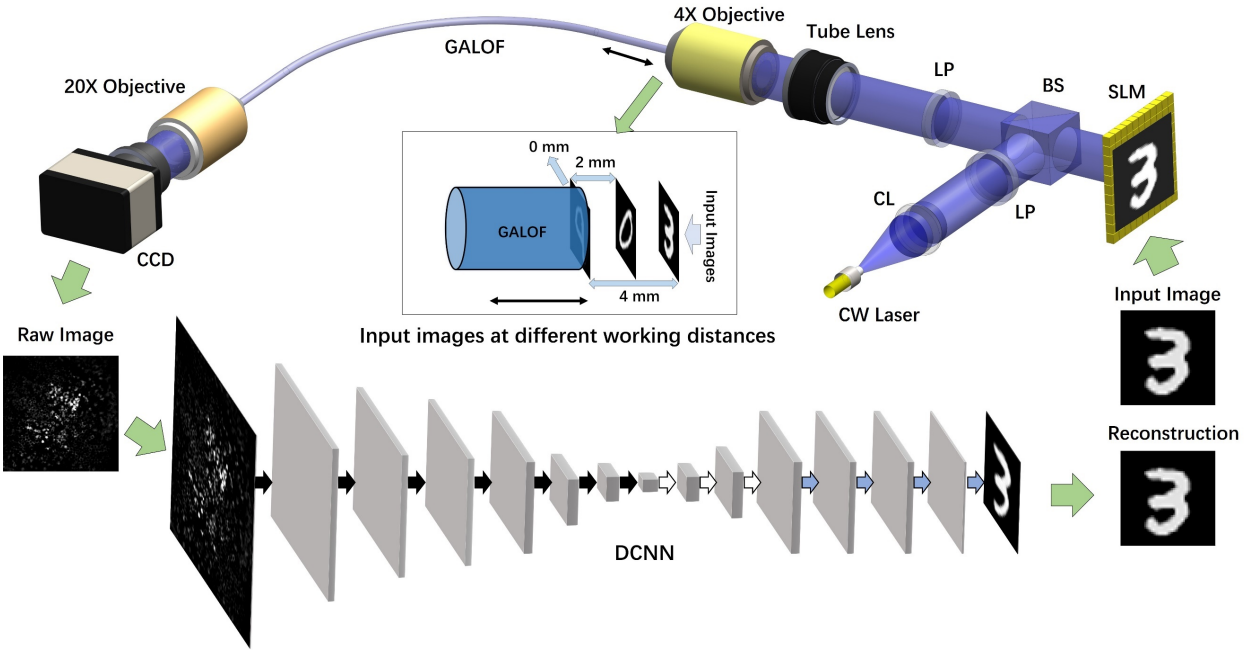

Figure 12. Schematic of deep-learning based imaging experimental setup and procedure. CW Laser: 405 nm laser diode, CL: collimating lens with 50mm focal length, LP: linear polarizer, BS: beam splitter.

We apply the DCNN to address the challenges facing GALOF-based FOISs. We demonstrate that the imaging quality is improved by the DCNN to the artifact-free level. In particular, by combing the bending-independent properties of the GALOF with DCNN based reconstruction, meter-long distance fully flexible imaging transportation is achieved. Moreover, the DCNN+GALOF scheme does not need any distal optics to transport 2D imaging information at various working distances. Therefore, the diameter of the FOIS could be reduced to the diameter of the fiber itself. In addition, we also prove that the DCNN+GALOF scheme can predict the depth of imaging objects precisely.

The experimental setup is shown in Fig. 12. The total length of the GALOF is 90 cm. For our object generation, we use 405 nm laser light that is delivered by an SMF and collimated by a lens. An SLM is located in between two linear polarizers to create an intensity object using its individual pixels. The light goes through the first polarizer oriented at 45° with respect to the extraordinary axis of the SLM. After reflection from SLM, the beam transmits through the second polarizer with the same polarization orientation as the first one. The SLM pixel size is 9.2×9.2 μm^2, and the number of pixels is 1920×1152. The SLM is modulated by 8-bit grayscale input images obtained from the MNIST database of handwritten digits. The images created with the SLM are resized to a matrix of 56×56 pixels. Subsequently, the SLM images are de-magnified by a factor of 4 and projected onto the GALOF input facet by the combination of a tube lens and a 4x objective. At the output end of the GALOF, the fiber facet is projected onto a CCD camera (Manta G-145B) by a 20x objective. The CCD pixel size is 6.45×6.45 μm^2, and the number of pixels is 1388×1038. We crop the collected raw images to an 896×896 square for processing. We repeat the experiments for both straight and bent GALOF (90-degree bend) as well as different imaging depths. To modify the imaging depths, we move the position of the bare fiber input end so that the distance between fiber input facet and the imaging plane is changed from 0 mm to 4 mm. For each experiment, a large number of matched input images and raw images pairs are applied to train the DCNN model. In the training phase, parameters of the DCNN are optimized to build a suitable computational architecture. Then, a separate set of image pairs serves as a test set to evaluate the performance of the trained DCNN. When collecting data, we first send 4000 different input images to the SLM and record the corresponding raw images with the CCD camera. These 4000 image pairs, originally generated by the SLM and their corresponding CCD-recorded raw images, are

used as the training set. Using the same set-up, we collect another 500 pairs of different images that serve as our test set for the image reconstruction analysis. In both training and test phase, the MAE is applied as the metric.

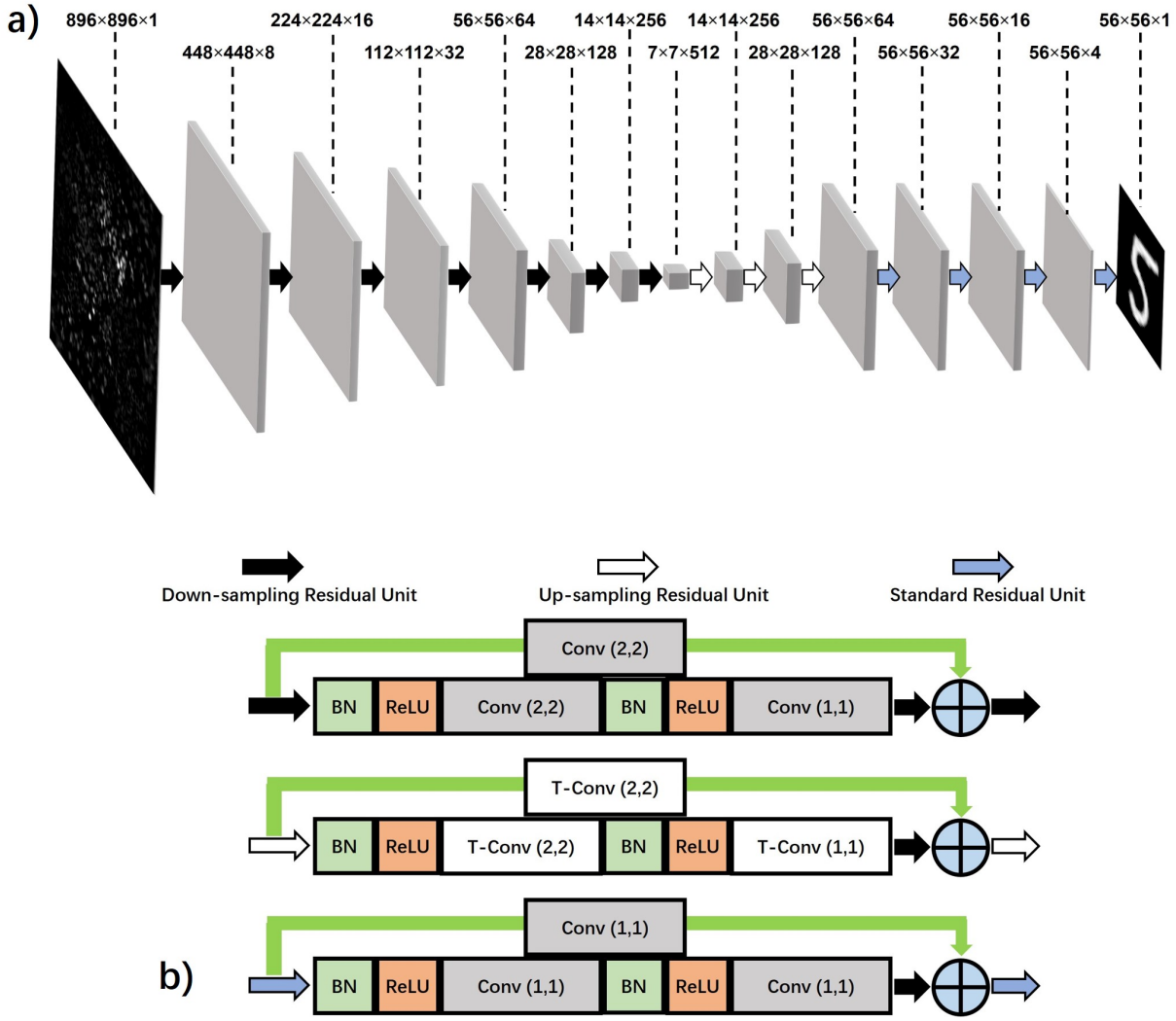

Figure 13. The architecture of DCNN for image reconstruction. a) The structure of the DCNN. b) Details of the residual units corresponding to arrows with different colors (BN: Batch Normalization, ReLU: Rectified Linear Unit, Conv: Convolution, T-Conv: Transposed Convolution).

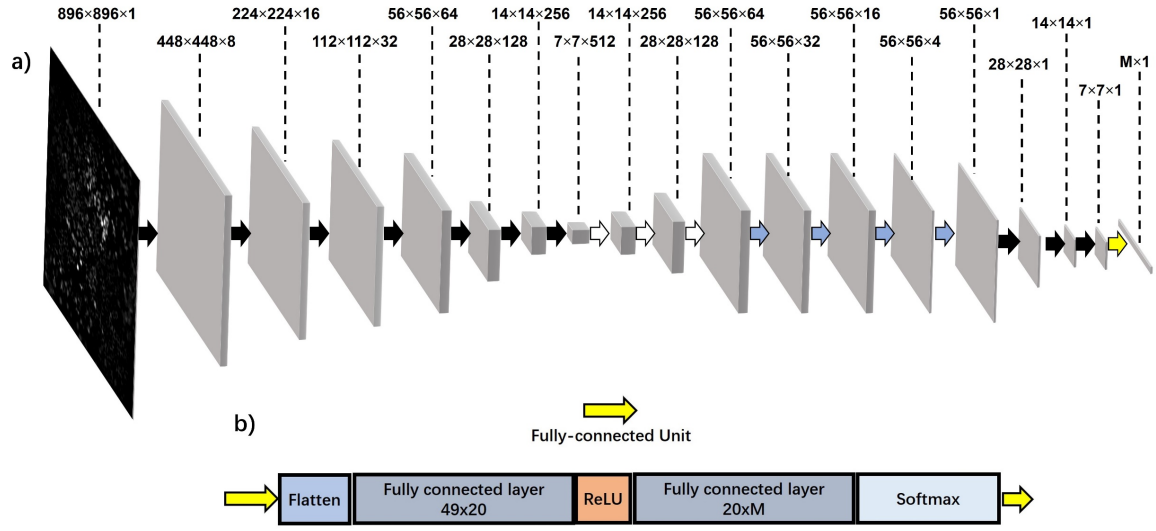

Figure 14. The architecture of the DCNN for depth prediction. a) A detailed structure of the DCNN. b) The detail of the fully-connected Unit.

Our DCNN for imaging reconstruction uses a convolutional residual neural network architecture, as shown in Fig. 13 a). The gray cubes represent the imaging data which are three-dimensional matrices, and the arrows with different colors stand for different types of residual units. The input of the network is the raw image with a size of 896×896×1. After 7 down-sampling residual units, the neural network extracts high dimension features from the raw image with a size of 7×7×512. Subsequently, three up-sampling residual units followed by another 4 standard residual units re-construct the final output which represents an estimation of the original input image. As shown in Fig. 13 b), the residual units consist of batch normalization layers, Relu layers, convolutional layers and skip connections. The skip connection enables smooth propagation in the DCNN and eases the training process. The batch normalization layer suppresses the internal covariance shift, allows higher learning rates and accelerates the training process. The function of the Relu layer is to add nonlinearity, while the convolutional layers connect adjacent layers by convolution. In our network, we set all convolutional filters as 3×3. The stride of the convolution

operation in all convolutional layers and skip connections are labeled in the residual units as shown in Fig. 13 b). To optimize the network parameters, we first initialize the network weights using a Gaussian distribution. Then we define the loss function which we aim to minimize. The loss function of our network is defined as:

$$L_{rec} = \frac{1}{wh}\left\|I_{rec} - I_{obj}\right\| + \frac{\lambda}{2}\sum_{i,j}\left\|W_{i,j}\right\|_2^2 \tag{11}$$

where the first term is a measure of similarity, the MAE between the reconstructed and the input object images. w and h are the width and height of the images, respectively. The second term is a L_2 regularizer of the network introduced to prevent overfitting. $W_{i,j}$ is the j^{th} weight in the i^{th} unit of the network. λ is a regularization constant which is set to 0.0001. In each update, we calculate the loss according to equation (11) and then propagate the gradient of the loss back to obtain the gradient with respect to each weight in the network. The network weights are updated with an ADAM optimizer from the gradients to minimize the loss over 4000 training imaging pairs. The learning rate is set to 0.001. The batch size is set to 80. The neural network is trained for 60 epochs with shuffling of the training samples between each epoch. The training procedure takes about 38 minutes using two GPUs (NVIDIA GeForce 1080Ti). The reconstruction time is only 4 ms for each test image. This shows the potential to perform *in vivo* video-rate real-time reconstruction of moving samples such as cells or neurons.

The problem of predicting the imaging depth is formulated as a classification model. The architecture of the DCNN for depth prediction is shown in Fig. 14 a). The first 14 residual units are the same as in the DCNN for imaging reconstruction shown in Fig. 13 a). They are followed by another three down-sampling residual units and a fully-connected unit. The input is the raw

image, and the output is an $M\times1$ vector containing the predicted probability for M possible depth. The summation of all M possibilities is 1. The underlying rationale is to predict the depth based on the reconstructed intermediate image. For the 90 cm-long GALOF sample, the objects are located at three depth, 0 mm, 2mm and 4 mm. For the 4.5 cm-long GALOF sample, we collect data at 6 different depths ranging from 0 mm to 10 mm with a step of 2 mm. Therefore, M equals 6 for the short sample and 3 for the long sample. The details of the fully-connected unit are demonstrated in Fig. 14 b). The "Flatten" layer reshapes the output of the forward layer from a $7\times7\times1$ matrix to a 49×1 matrix. This is followed by two fully connected layers, one Relu layer, and one Softmax layer, before the output of an $M\times1$ vector is obtained. To optimize the network parameters, we first initialize the network weights again using a Gaussian distribution. Then we define the loss function which we aim to minimize. The loss function of CNN-Depth is defined as:

$$L_{depth} = -\frac{1}{N}\sum_{n=1}^{N}\sum_{c=1}^{M} y_c \log(p_c) + \frac{\lambda}{2}\sum_{i,j}\left\|W_{i,j}\right\|_2^2 \tag{12}$$

where the first term is the cross entropy which measures the accuracy of our model, and the second term is again an L_2 regularizer. N is the batch size, M is the number of possible depths, and y_c is a binary flag indicating the truth of the depth label of the object. If the depth label c is the correct label for the current measurement y_c is set to 1, or else it is set to 0. p_c is the predicted probability value for the depth label c. For this loss function, the regularization constant λ is set to 0.0001. We start the training process by uploading the raw images to the network and obtain the loss. Then we propagate the gradient of the loss function back to obtain the gradient with respect to each weight. The network weights are updated with an ADAM optimizer to minimize the loss function. The learning rate is set to 0.0001. The batch size is set to 200. The neural network is trained for 150

epochs with shuffling of the training samples between each epoch. We train the DCNN by 6000 and 12,000 training imaging pairs for the 90 cm-long sample and 4.5 cm-long sample, respectively. In the test phase, we utilize 900 and 1800 images as test sets for the long sample and short sample, respectively.

4.2 Results and Discussions

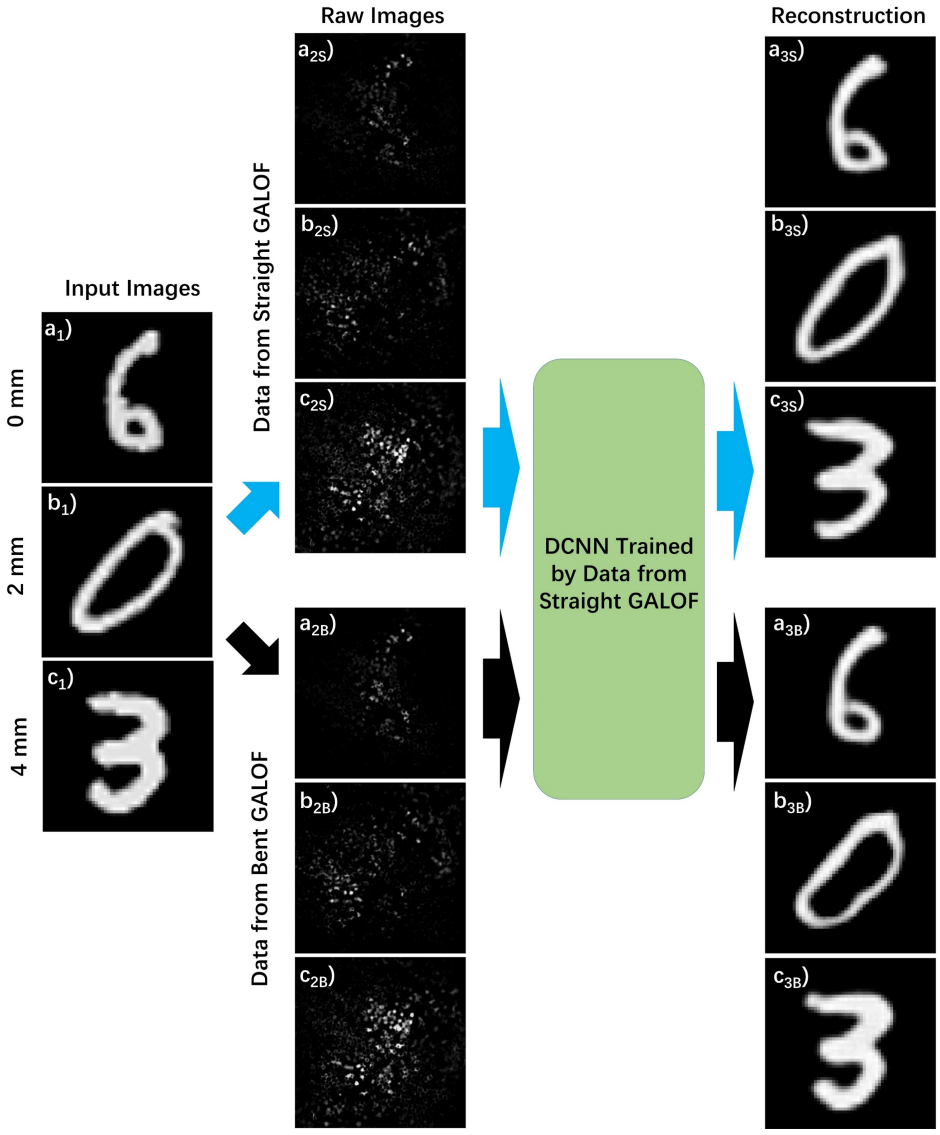

Figure 15. Image reconstruction results. a_1)-c_1) Three test input images located at different working distances, ranging from 0 mm to 4 mm. The blue arrow and black arrow indicate the reconstruction processes for data collected from the straight and the bent state of the same 90 cm-long GALOF sample, respectively. For the bent state, the bending angle is 90°. The DCNN used here is trained just once by the training data collected from the straight fiber. a_{2S})-c_{2S}) Raw intensity images collected from the straight fiber. a_{2B})-c_{2B}) Raw intensity images collected from the bent fiber. a_{3S})-c_{3S}) Reconstructed images from raw intensity images a_{2S})-c_{2S}). a_{3B})-c_{3B}) Reconstructed images from raw intensity images a_{2B})-c_{2B}). a_{2S})-a_{3S}) and a_{2B})-a_{3B}) are obtained when the working distance is 0 mm. b_{2S})-b_{3S}) and b_{2B})-b_{3B}) are obtained for 2 mm working distance. c_{2S})-c_{3S}) and c_{2B})-c_{3B}) are obtained for 4 mm working distance.

Sample reconstruction results from raw images measured after transport through straight GALOF are shown in Fig. 15 a_{3s})-c_{3s}). The data shown in Fig. 3 indicated by blue arrows are collected with straight fiber at different imaging depths, ranging from 0 mm to 4 mm. The DCNN used for reconstruction at the three different depths is the same. However, the DCNNs are trained for each depth individually resulting in depth-specific DCNN parameters. Comparing input images and the corresponding reconstructed images, it is apparent that our trained DCNNs are able to recover the true images remarkably well. Moreover, the imaging plane of our system is not limited to a specific depth. Without extra distal end optics, for objects located between 0 mm and 4 mm from the fiber facet, our system can perform high-quality image transportation and reconstruction. An object distance of 4 mm represents an order of magnitude improvement compared to most recently reported FOISs [35, 49, 52]. Being able to image objects at a considerable distance from the fiber facet without any imaging elements will potentially reduce the size of the imaging device to the diameter of the fiber itself. Therefore, FOISs based on our system can be operated in a minimally invasive manner dramatically decreasing the risk of damage, for instance, to human organs. This is also important in *in vivo* studies of neural activity since there is a good chance to damage the neurons close to the fiber tip. We also demonstrate reconstruction results of ten different writing styles of the same number "5" at three different depths, see Fig. 16-Fig. 18. These demonstrated high-quality reconstructions for different depth can only happen when the neural network has learned both the inverse operator and the prior. In other words, the neural network has learned the underlying physics. Hence, although the objects from the MNIST database are relatively simple, there should be no limitations on the complexity of the objects for the imaging system to perform well.

The DCNN trained to reconstruct images from the straight fiber can be used directly to perform reconstruction for bent GALOF. As is indicated by black arrows in Fig. 15, this bending independence of the DCNN+GALOF imaging system also applies to large imaging depths. Since bending independence is mainly due to the single-mode properties of the transmission channels embedded in the GALOF, the transmission should stay the same for arbitrary bent states. Without loss of generality, we bend the GALOF by 90 degrees and collect the test raw imaging data for object depths of 0 mm, 2mm, and 4mm, respectively. As illustrated in Fig. 15 a_{3B})-c_{3B}), high-quality images can be recovered by feeding raw test images of low quality into the DCNN model. Please note that these raw test images of different depth are obtained after transport through bent GALOF while the DCNN training was performed using straight GALOF

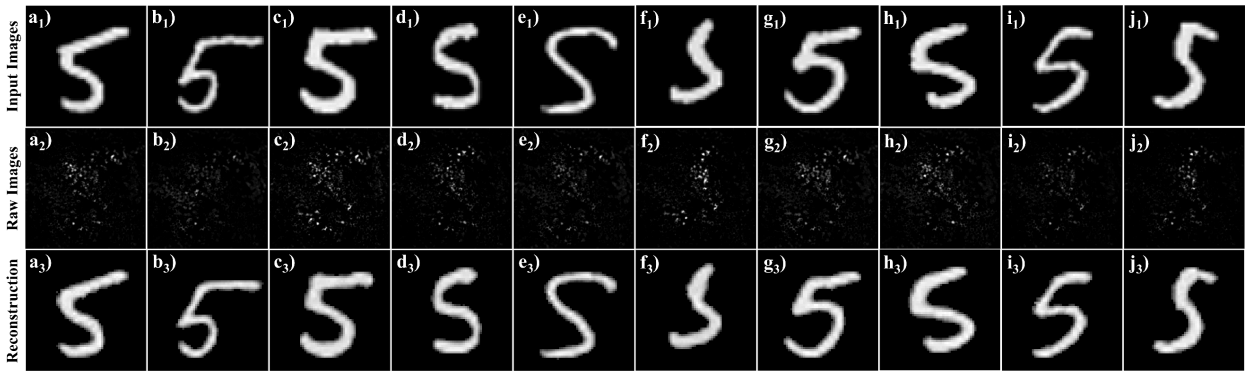

Figure 16. Reconstruction of number "5" with 10 different writing style from the MNIST database at 0mm imaging depth. a_1)-j_1) are input object images; a_2)-j_2) are the corresponding raw intensity images transmitted through a 90-cm long straight GALOF; a_3)-j_3) are reconstructed images from the raw images.

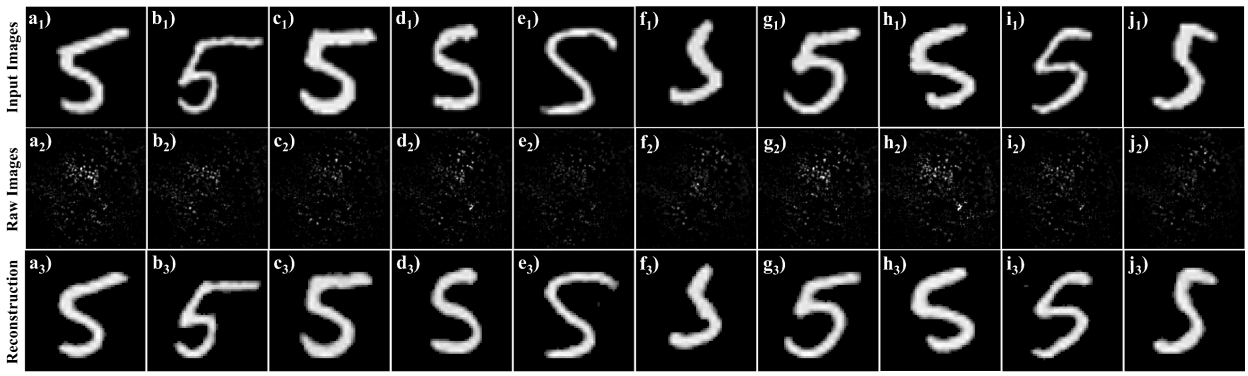

Figure 17. Reconstruction of number "5" with 10 different writing style from the MNIST database at 2mm imaging depth. a_1)-j_1) are input object images; a_2)-j_2) are the corresponding raw intensity images transmitted through a 90-cm long straight GALOF; a_3)-j_3) are reconstructed images from the raw images.

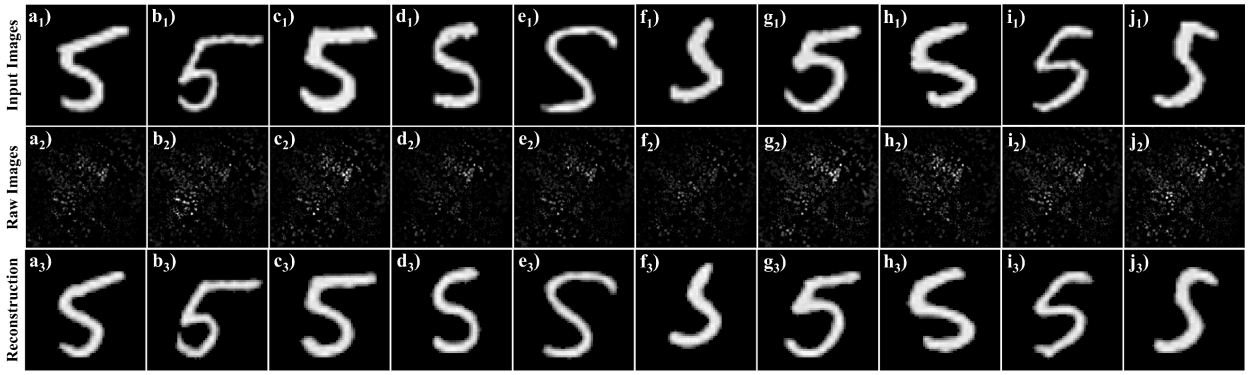

Figure 18. Reconstruction of number "5" with 10 different writing style from the MNIST database at 4mm imaging depth. a_1)-j_1) are input object images; a_2)-j_2) are the corresponding raw intensity images transmitted through a 90-cm long straight GALOF; a_3)-j_3) are reconstructed images from the raw images.

For quantitative analysis, bar graphs are plotted in Fig. 19 that show the normalized MAE and its statistics for test data sets of different depths transferred through straight (yellow bars) and bent GALOF (green bars). The low-test errors for all cases suggest that our DCNN has learned the physics model of the imaging system and can generate highly accurate results. The slightly higher test error for bent fiber might be attributed to the experimental process that requires movement and re-adjustment of the imaging setup located at the output side. For other FOISs, such as MMF-

based fiber imaging, a few hundred micrometers perturbations are already strong enough to impair the image quality. For MCF-based fiber imaging, bending of the fiber can also mess up the imaging process if TM approach is applied. Compared to that extreme bending-sensitivity of other advanced FOISs, our system is totally free from the impact of strong bending. This ability would make our system an ideal candidate for a fully-flexible medical endoscope used in clinical diagnostics.

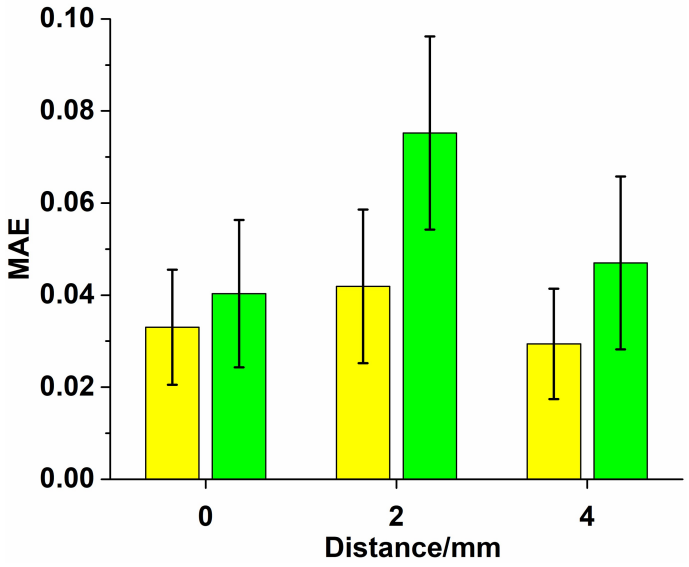

Figure 19. The error analysis for both straight GALOF and bent GALOF. Yellow and green bars correspond to the cases without and with bending, respectively.

We also explore the possibility of predicting the depth of an object using GALOF-transported raw images. For this purpose, we apply the DCNN classification model shown in Fig. 14. After finishing the training process, this DCNN is able to predict the image depth within a particular depth set, here 0 mm, 2 mm and 4 mm. The input images corresponding to different depth are randomly mixed, then the trained DCNN can still predict the depth of the images with an average

accuracy of 98.66% for the 90 cm-long GALOF, see Fig. 20 a). We also study the depth prediction capability of our system using a separate 4.5 cm-long GALOF sample, where we report the sorting of images into six depth categories ranging from 0 mm to 10 mm. The test results for the short sample are summarized as a confusion matrix shown in Fig. 20 b). The value of the different colors in the matrix is the probability of prediction for a certain depth. The averaged probability of accurately predicting the depth is 86.29 % for this short GALOF sample. Beyond the demonstrated ability to obtain high-quality images of objects that are several millimeters away from the bare fiber facet, the depth prediction capability provides a first step towards the reconstruction of images with a remarkable depth resolution.

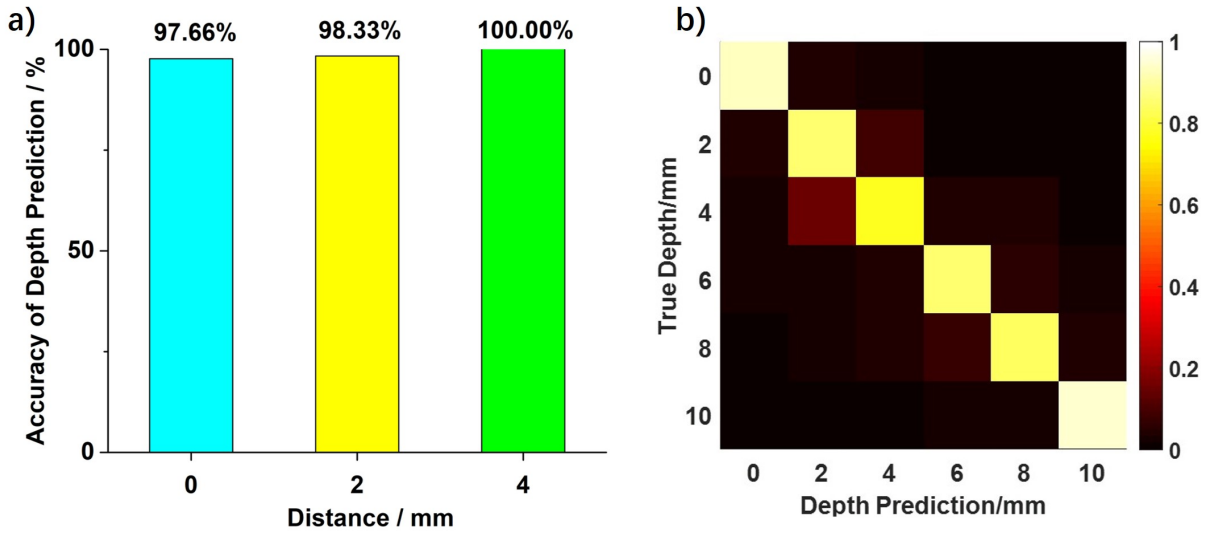

Figure 20. Depth prediction results. a) The probability that the DCNN in Fig. 14 a) can recognize correctly the three different imaging depths (0mm, 2mm, 4mm) from the measured raw images using a 90 cm-long GALOF sample. b) Confusion matrix of object depth prediction using a 4.5 cm-long GALOF segment for image transfer.

The DCNN shown in Fig. 13 a) is also able to transfer its learning capability to reconstruct objects that belong to classes different from the training objects. We reconstruct English letters

with different writing styles using the same DCNN model trained by a straight GALOF and the MNIST database of handwritten digits. English letters are a member of a totally different domain compared to the numbers in the MNIST dataset. We pick the letters "CREOL" as the object. The image size of the object is 112×200 pixels. Limited by the size of the GALOF diameter, we have to scan the object and stitch the subsets together to obtain the complete images shown in Fig. 21 a_1) and b_1). The comparison between the reference and the recovered image demonstrates that our system is able to accurately reconstruct images belonging to a very different class. This is further strong evidence that our DCNN is an accurate estimate of the physics model. Therefore, the imaging capability of our system generalizes well through objects of different classes. In addition, although the demonstrated results are mainly based on handwritten numbers and English letters, imaging targets of DCNN-base GALOF systems are not limited to binary and sparse objects.

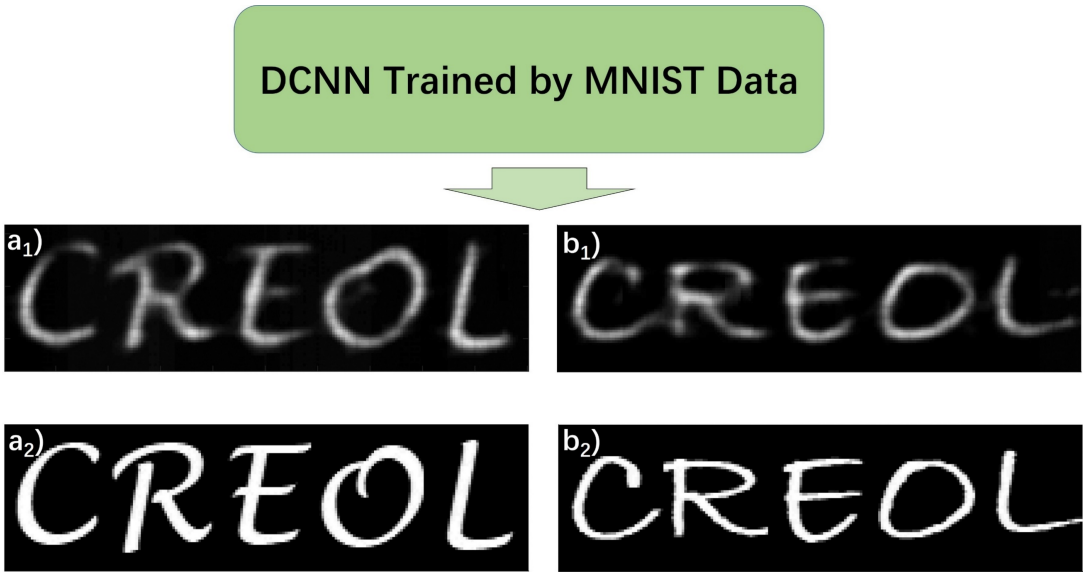

Figure 21. Transfer-learning reconstruction of English letters with two different writing styles. a_2) and b_2) Input image. The working distance is 0 mm and the GALOF is kept straight. "CREOL" is short for "College of Optics and Photonics". The size of the input image is 56×200 pixels. a_1) and b_1) Reconstructed images corresponding to a_2) and b_2), respectively.

In conclusion, we demonstrate a fully-flexible and artifact-free fiber-based imaging system with a meter-long GALOF at multiple working distances up to several millimeters. There are several fundamental aspects that set our system apart from other approaches, most notably the bending independence of the network training process and the large object depth that has been achieved without the need for distal optical elements. Our system's tolerance to flexible bending and long working distances will be of enormous benefit for both basic research on biological and disease processes and practical application in clinical diagnostics and surgical operations.

CHAPTER FIVE: DEEP LEARNING CELL IMAGING

The DCNN-GALOF fiber imaging system discussed in chapter four is faced with several challenges limiting its practical application. First, the system only demonstrated success in imaging of low-resolution sparse objects, such as the binary MNIST handwritten numbers. There is a chasm between spare objects reconstruction and the reconstruction of biological objects which are typically different types of cells or tissue with complicated morphologic features. Very recent research on the GALOF shows that there exist high-density localized modes with nearly diffraction-limited wavefront quality and high spatial coherence [27]. These modes distribute uniformly across the random structure in the GALOF. This shows the great potential of GALOFs to perform imaging on complex biological objects. Also, in order to accomplish the demanding task to resolve and reconstruct the subtle details of a biological object, new-designed DCNNs which can "learn" the underlying physics of imaging process with much higher precision and tolerance are required. Second, the demonstrated transfer-learning capability of the previous DCNN-GALOF system was limited to binary sparse testing objects that were quite similar to the objects in the training data [15, 64]. It would be more confirmative if the system would feature transfer learning performed using objects with features very different from the training data. Third, it is still unknown if the DCNN-GALOF system could perform high-quality imaging under incoherent broadband illumination. The ability to perform imaging under incoherent broadband illumination is an important step towards practical applications due to following aspects. 1) In medical applications, some medical practitioners might prefer incoherent broadband illumination. For example, white-light transmission cellular micrographs are already very familiar to histopathologists [33, 41]. 2) The coherence of lasers results in speckle patterns which reduce the

image quality. In addition, the high intensity of laser light might be damaging to biological objects such as living cells and the cost of lasers is relatively high. Comparing to laser light source, incoherent illumination, such as LED illumination, can generally give better imaging quality without speckle patterns. The low intensity of incoherent light also helps protect cells against photobleaching and phototoxicity during the imaging process. At the same time, the cost of LEDs is much lower compared to laser systems [74]. Currently, most state-of-the-art MCF- or MMF-based systems cannot handle incoherent broadband light source due to the inherent limitation of the wavefront-shaping TM method and the properties of MCF and MMF. In contrast to that, DCNN itself does not raise any requirements on illumination. Moreover, very recent research progress unveils that localization lengths of localization modes are shown to be independent of wavelength [28]. It means the point spread function of the GALOF is not affected by broadband illumination. Therefore, unlike MCF and MMF, the GALOF itself has the ability to support imaging process using broadband light. Since both DCNN and GALOF shows compatibility with incoherent broadband illumination, it should be possible to develop a novel incoherent DCNN-GALOF system.

To resolve all abovementioned issues, we develop an incoherent light illuminated DCNN-GALOF imaging system with the capability to image various cell structures. Within this system, a new C-DCNN model with a tailored design is applied to the image reconstruction process, and a low-cost LED works as the light source. We call the new system Cell-DCNN-GALOF. We demonstrate that it is able to transfer high quality, artifact-free images of different types of cells in real time. We further prove that the imaging depth of this system can reach up to several millimeters without any distal optics. In addition, we show that the image reconstruction process

is remarkably robust with regard to external perturbations, such as temperature variation and fiber bending. Last but not least, the transfer-learning capability of the new system is confirmed by using cells of different morphology for testing. The work presented here introduces a new platform for various practical applications, such as neuroscience research and clinical diagnosis. The system performance of the Cell-DCNN-GALOF is superior to most recent reported similar systems. It is also a new cornerstone for imaging research based on waveguide devices using transverse Anderson localization.

5.1 Experimental Procedure and C-DCNN

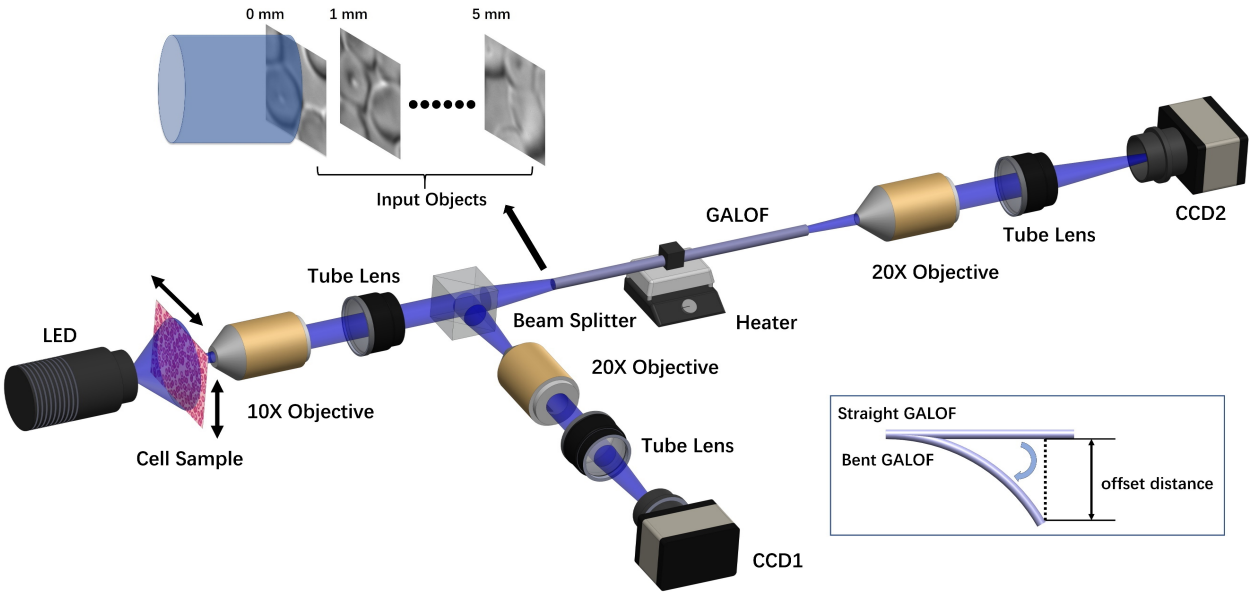

Figure 22. Schematic of the cell imaging setup.

The experimental setup is shown in Fig. 22. The light source is a LED with a center wavelength of 460 nm. An 80 cm long GALOF sample is utilized. The images of cell samples are magnified by a 10x objective with a NA value of 0.3 and split into two copies sent into a reference path and a measurement path, respectively. The cell samples are scanned both vertically and horizontally with 5 μm steps to obtain training, validation and test data sets. In the reference beam path, the image is further magnified by a 20x objective (NA=0.75) and recorded by CCD 1 (Manta G-145B, 30 fps) after passing through a tube lens. In the measurement path, the image is transported through the 80 cm long GALOF and then projected onto CCD 2 (Manta G-145B, 30 fps) by the same combination of 20x objective and tube lens. Reference images and raw images of different areas of cell samples are recorded by CCD 1 and CCD 2, respectively, while the samples

are being scanned. The reference images are labeled as the ground truth. Both reference and raw images are 8-bit grayscale images and are cropped to a size of 418x418 pixels.

Experiments are performed for both straight GALOF and bent GALOF. To quantify the amount of bending, the offset distance is measured which is defined as the distance from the end of the bent fiber to the position of the straight fiber (equal to the length of the dashed line). To bend the fiber, the input end of the GALOF is fixed while the output end of the GALOF is moved by an offset distance d. The relation between the offset distance and the corresponding bending angle of the fiber θ is given by $d=L[1-\cos(\theta)]/\theta$, where L is the total length of the GALOF. Besides the bending test, the robustness of the imaging system is also investigated under different temperatures. In the experiments of testing the imaging system tolerance with regard to thermal variations, a 10 mm-long section in the middle of the GALOF is heated. The temperature of a GALOF segment can be tuned by the heater underneath. Cell imaging at various depth is also performed using this setup. As shown in the inset above the setup in Fig. 22, the images of cells located at different imaging planes are collected by the bare fiber input end. The distance between the image of the object and the fiber input facet is defined as the depth. Initially, the image of the object is received by GALOF's input facet with 0 mm. Then, the imaging depth is increased with a step of 1 mm by moving the fiber input end through a translation stage. The depth ranges from 0 mm to 5 mm.

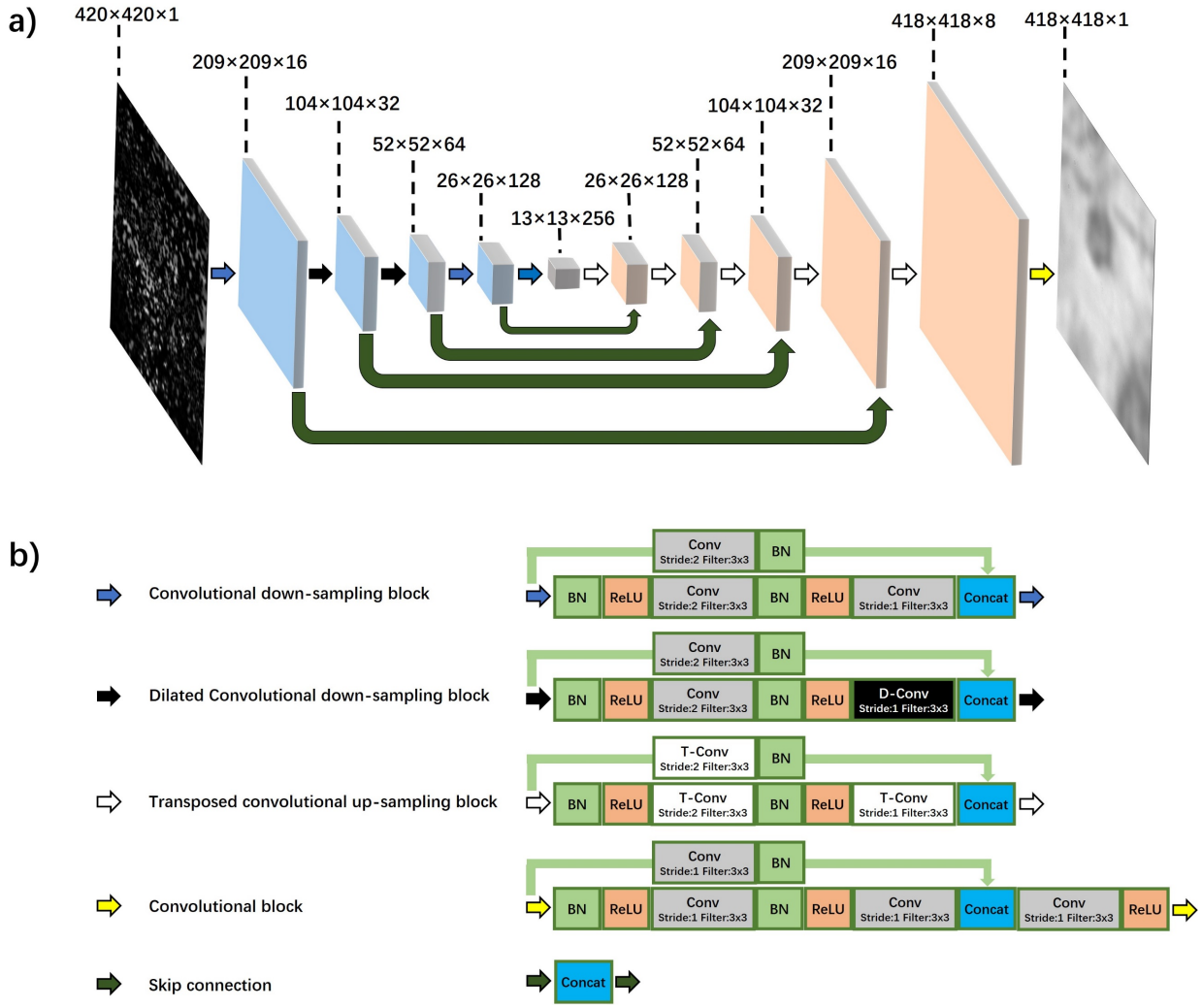

Figure 23. The architecture of the C-DCNN. a) The detailed structure of the C-DCNN. The raw image which is resized to 420x420 using zero padding is the input layer. The input layer is decimated by five down-sampling blocks (blue and black arrows) to extract the feature maps. Then five up-sampling blocks (white arrows) and one convolutional block (yellow arrow) are applied to reconstruct the images of cell samples with a size of 418x418. The skip connections (dark green arrows) pass feature information from feature-extraction layers to reconstruction layers by concatenation operations. The MAE-based loss metrics are calculated by comparing the reconstructed images with the reference images. The parameters of the C-DCNN are optimized by minimizing the loss. b) Detailed block operation diagrams corresponding to the respective arrows shown on the right side (BN: Batch Normalization, ReLU: Rectified Linear Unit, Conv: Convolution, D-Conv: Dilated Convolution, T-Conv: Transposed Convolution, Concat: Concatenation).

The details of our new C-DCNN is shown in Fig. 23. The Keras framework is applied to develop the program code for the C-DCNN. The regularization applied in the C-DCNN is defined by the L_2-norm. The parameters of the DCNN are initialized by a truncated normal distribution. For both training and evaluation, the MAE is utilized as the metric. Adam optimizer is adopted to minimize the loss function. During the training process, the batch size is set at 64 and the training is run through 80 epochs with shuffling at each epoch for all the data shown in this paper. The learning rate is set at 0.005. Both training and test process are run in parallel on two GPUs (GeForce GTX 1080 Ti).

5.2 Results and Discussions

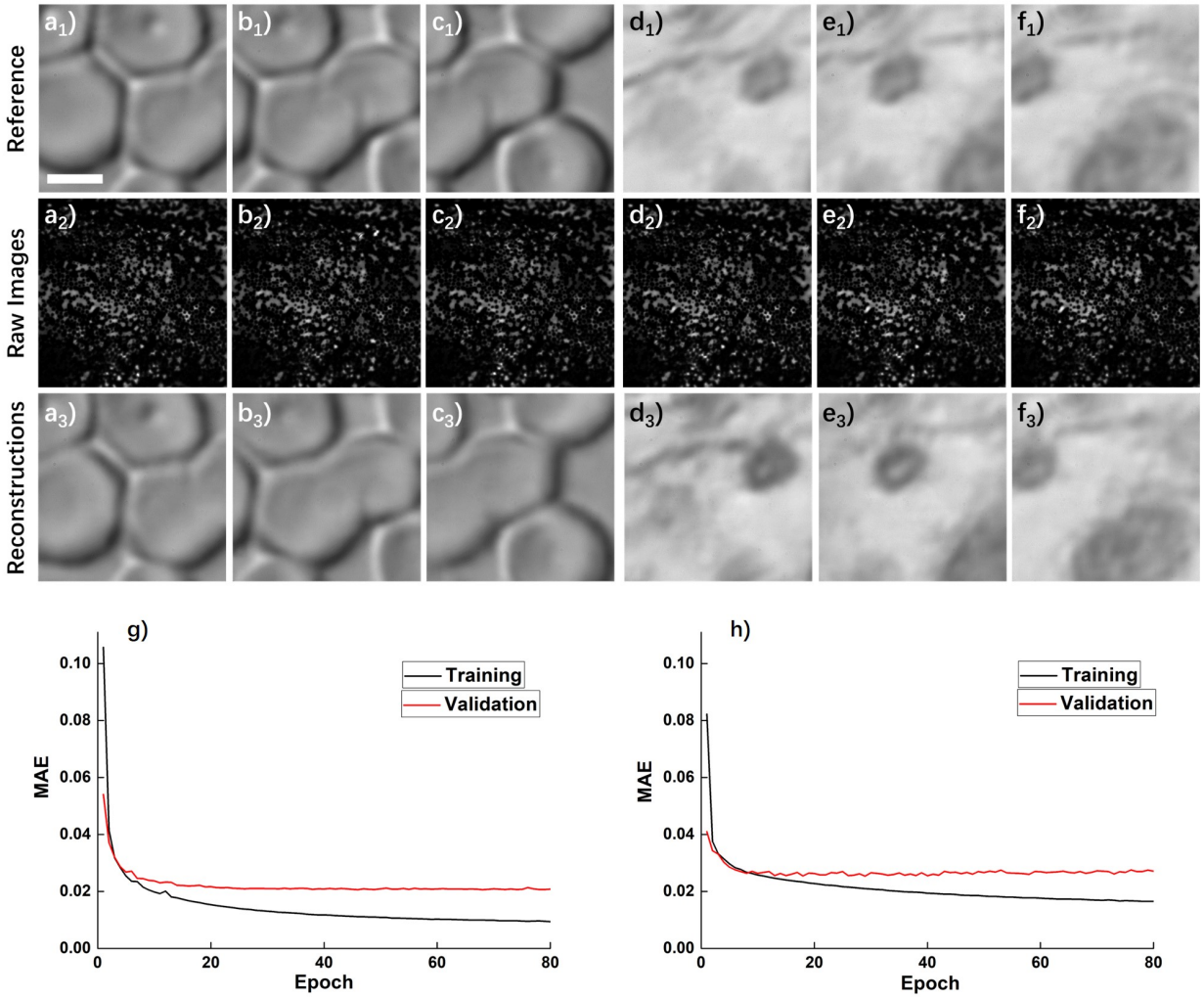

Figure 24. Cell imaging of different types of cells. a)-c) are test data for human red blood cells. d)-f) are test data for cancerous human stomach cells. All data are collected with straight GALOF, at room temperature with 0 mm imaging depth. The length of the scale bar in a_1) is 4 μm. a_1)-f_1) are the reference images; a_2)-f_2) are the corresponding raw images. a_3)-f_3) are the images recovered from the raw images. g) and h) Accuracy improvement curves during the training process. g) shows the accuracy improvement curves for training and validation using imaging data of human red blood cells; h) shows the accuracy improvement curves for training and validation using imaging data of cancerous human stomach cells.

To demonstrate the imaging reconstruction capability, two different types of cells, human red blood cells and cancerous human stomach cells, serve as objects. By scanning across different areas of the cell sample, we collect 15000 reference and raw images as the training set, 1000 image pairs as the validation set, and another 1000 image pairs as the test set for each type of cell. During the first data acquisition process, the GALOF is kept straight and at room temperature of about 20°C. The imaging depth is 0 mm, meaning that the image plane is located directly at the fiber input facet. The training data are loaded into the C-DCNN to optimize the parameters of the neural network and generate a computational architecture that can accurately map the fiber-transported images to the corresponding original object. After the training process, the test data are applied to the trained model to perform imaging reconstruction and evaluate its performance using the normalized MAE as the metric. In the first round of experiments, we train and test each type of cell separately. With a training data set of 15000 image pairs, it takes about 6.4 hours to train the C-DCCN over 80 epochs on two GPUs using a personal computer. The accuracy improvement curves for both training and validation process over all 80 epochs are provided in Fig. 24 g) and h). After training, the reconstruction time of a single test image is about 0.05 second. Figs. 24 a)-f) show some samples from the test data set. In a) to c), reference images, raw images, and recovered images of three in succession collected and reconstructed images of human red cells are shown, while in d) to f) three images of cancerous stomach cells are presented. Comparing the reference images with the reconstructed images, it is clear that the separately trained C-DCNNs are able to reconstruct images of both cell types remarkably well. The averaged normalized test MAEs are 0.024 and 0.027 for the human red blood cells and the cancerous human stomach cells, respectively, with standard deviations of 0.006 and 0.011. Further Fourier-transform analysis using

sample image of Fig. 24 a_3) shows that most high spatial frequency components of the reconstructed image are within the cut-off spatial frequency of the experimental setup, see Fig. 25. Due to fast imaging acquisition speed, we can visualize the test process for these two cell types through real-time video. This real-time imaging capability is highly desirable for many practical applications, such as *in situ* morphologic examinations of living tissues in their native context for pathology [33].

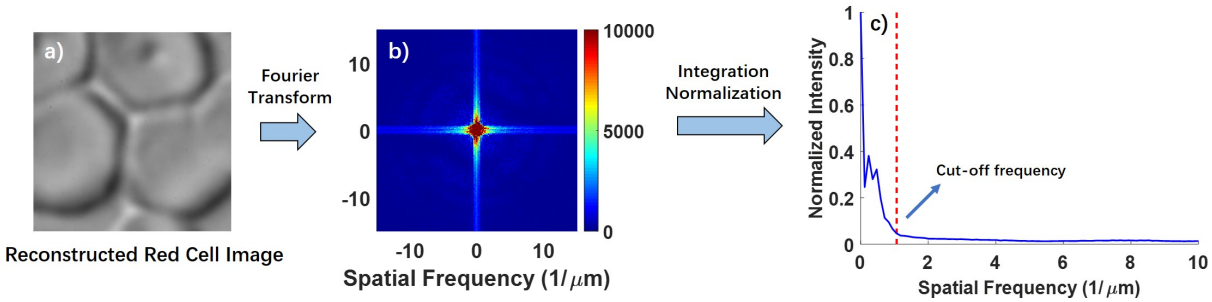

Figure 25. Analysis of C-DCNN-reconstructed image. a) Sample reconstructed red cell image from Fig. 24 a_3). b) Intensity image in the frequency domain. b) is obtained through a Fourier transform of a). c) is obtained by integrating along the radial direction of b). Data in c) is normalized. The red-dashed line in c) corresponds to the cut-off frequency of the experimental setup. It is estimated through ~ NA÷(0.61×wavelength). NA is equal to 0.3. The center wavelength of the light source, ~460nm, is used to estimate this cut-off frequency.

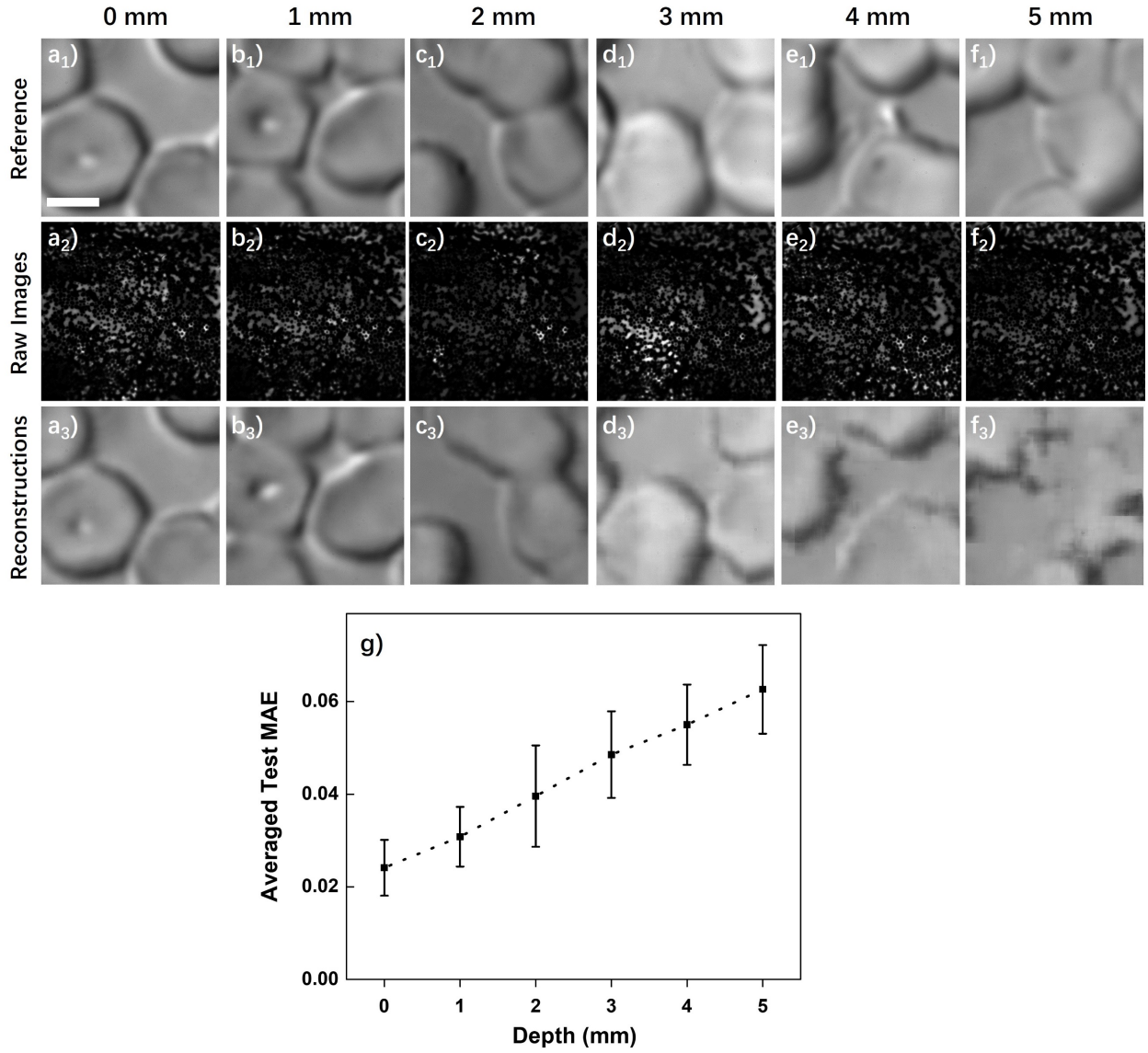

Figure 26. Multiple depth cell imaging. a)-f) are sample test data for human red blood cells. All data are collected with straight GALOF at room temperature. All three images in each column are from the same depth. The length of the scale bar in a_1) is 4 μm. a_1)-f_1) are the reference images; a_2)-f_2) are the corresponding raw images. a_2)-f_2) are obtained by varying the imaging depth from 0 mm to 5 mm with steps of 1 mm. a_3)-f_3) are the images recovered from the corresponding raw images. g) is the averaged test MAE error for each depth with the standard deviation as the error bar.

Distal optics located at fiber input end hinders conventional FOIS from miniaturizing the size of the imaging unit. Here, we are investigating the ability of our Cell-DCNN-GALOF system to

image objects located at various distances from the fiber input facet without distal optics. As illustrated in Fig. 22, the images of cells located at different imaging planes are collected by the bare fiber input end. The depth ranges from 0 mm to 5 mm with steps of 1 mm. For each individual depth, 15000 reference and raw images are collected as the training set, and another 1000 image pairs serve as the test set. The GALOF is kept straight and at room temperature during data collection. The C-DCNN is trained separately for each depth resulting in depth-specific parameters. Examining reference and reconstructed test images shown in Fig. 26 a) to f), high-quality image transmission and reconstruction can be achieved up to depths of at least 3 mm. The first visual degradation of the imaging quality appears around 4 mm and the visual quality of the reconstructed images drops further at 5 mm depth. The corresponding quantitative image quality evaluation is shown in Fig. 26 g). The normalized MAE increases almost linearly with a slope of about 0.008 per mm. Based on these data we conclude that our system can transfer high-quality cell images for objects being several mm away from the fiber input facet without the need for any distal optics. Therefore, the size of an image transmitting endoscope based on our system could be potentially minimized to the diameter of the fiber itself and the penetration damage could be reduced to a minimum without degrading the quality of the image of biological objects. The fiber could collect images of organs without touching them directly enabling a minimally invasive, high-performance imaging system.

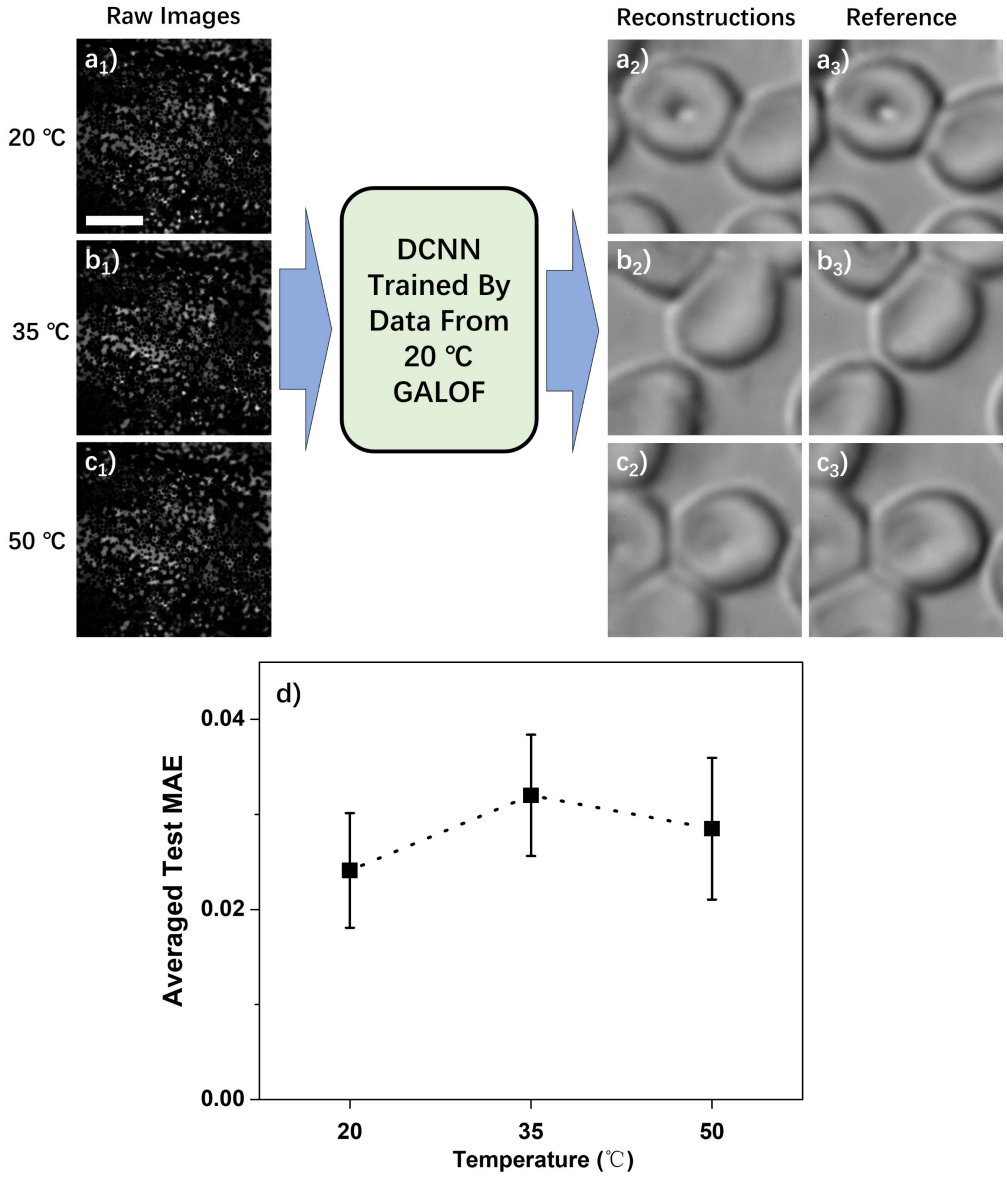

Figure 27. Cell imaging at different temperatures. a_1)-c_1) are test raw images of human red blood cells collected at 20 °C, 35 °C, and 50 °C, respectively. The length of the scale bar in a_1) is 4 μm. a_2)-c_2) are the images recovered from a_1)-c_1). a_3)-c_3) are the corresponding reference images. All data are collected with straight GALOF at 0 mm imaging depth. d) shows the averaged test MAE error for each temperature with the standard deviation as the error bar.

In practical applications, the optical fiber of the FOIS often needs to be inserted deeply into the cavity of living organs. This requires the imaging system to tolerate thermal variation and fiber

bending. For MMF-based FOIS, the increase of temperature or bending of the fiber when inserting fiber into organs or tissues induces strong variations of the mode coupling. These variations decrease the performance of MMF-based imaging systems due to induced changes of the TM [35]. This problem can be overcome by using GALOF since most of the modes embedded in GALOF show single mode characteristics which increases the system tolerance and can make it immune even to rather strong perturbations. We first investigate the effect of temperature variation on our Cell-DCNN-GALOF system by changing the temperature of a 10 mm long GALOF segment with a heater. During the data collection, we keep the GALOF straight and at 0 mm imaging depth. We collect 15000 image pairs at 20 °C as the training data. For test data, we record three sets of test data where the GALOF segment is heated to 20 °C, 35 °C, and 50 °C, respectively. Each set of test data consists of 1000 image pairs. The C-DCNN model is only trained by utilizing the training data collected at 20 °C. Subsequently, the trained model is applied to perform test image reconstruction of data acquired at all three different temperatures. In Fig. 27 a) to c), some sample images are shown. Comparing the reference with reconstructed images, the visual imaging quality is not affected by the thermal change even for a 30 °C variation. Most body temperatures of humans or animals fall into this range. This confirms the remarkable robustness of our Cell-DCNN-GALOF system regarding temperature fluctuations, which makes the system particularly suitable for *in vivo* imaging.

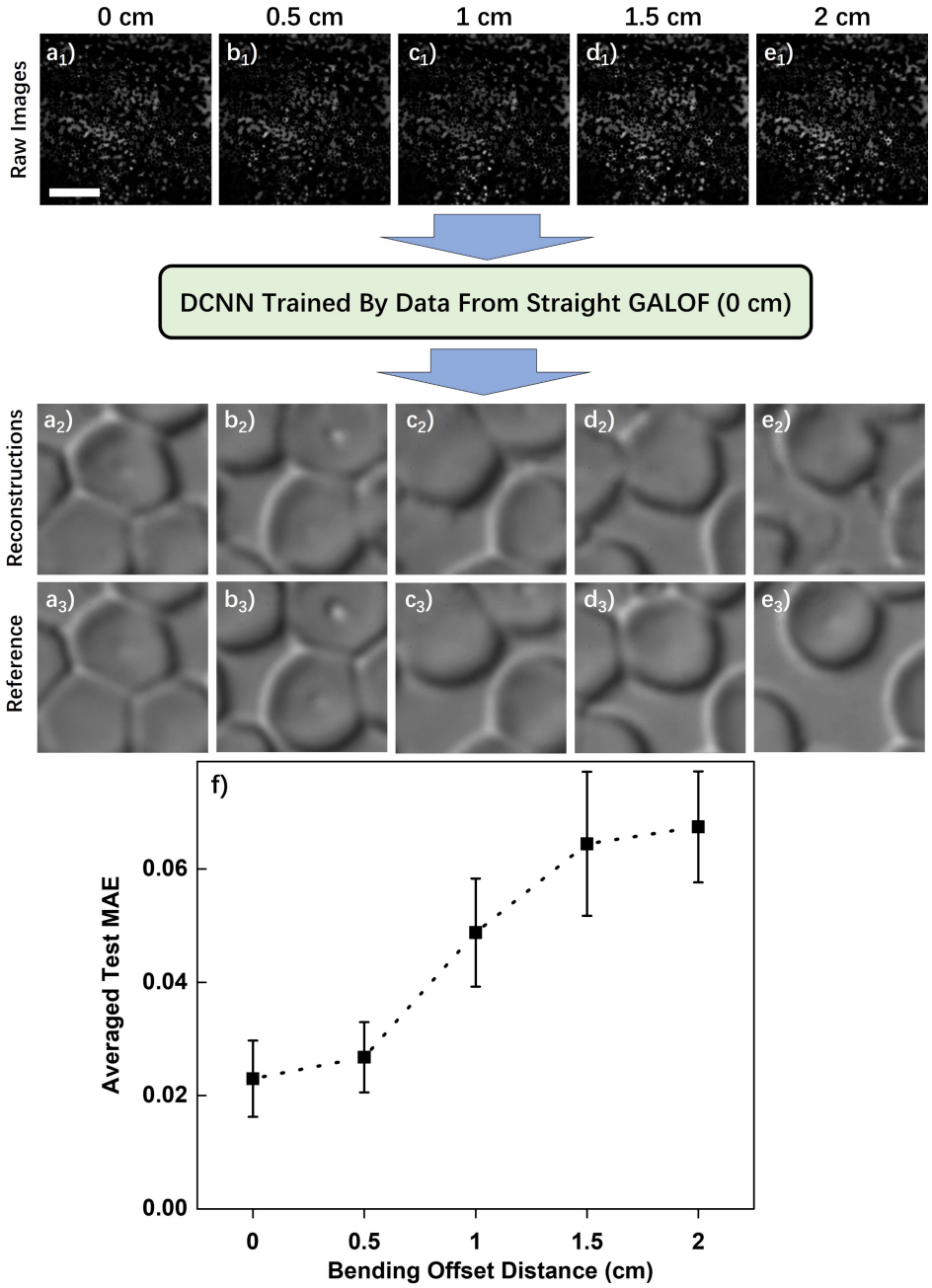

Figure 28. Cell imaging under bending. Data in each column in a)-e) correspond to examples with the bending offset distance listed above. The definition of offset distance is illustrated in Fig. 22. The bending angle range corresponding to offset distances between 0 cm and 2 cm is about 3 degrees. a_1)-e_1) are raw images collected at different bending offset distances. The length of the scale bar in a_1) is 4 μm. a_2)-e_2) are the images reconstructed from a_1)-e_1). a_3)-e_3) are the corresponding reference images. f) shows the averaged test MAE for five different bending states with the standard deviation as the error bar.

Next, we test the effect of fiber bending on the performance of our Cell-DCNN-GALOF system. We keep the temperature of the fiber at room temperature and the imaging depth at 0 mm. We collect 15000 image pairs with straight GALOF as the training data and record five sets of separate test data corresponding to five different bending states. Each test set consists of 1000 image pairs. Experimentally, the bending is induced by moving the fiber end by a specified offset distance as illustrated in Fig. 22. We first train the model only using the training data collected from straight GALOF. Then test images from all five different bending states are reconstructed by the non-bending-data trained C-DCNN model and evaluated using the MAE. The results are shown in Fig. 28. Based on the recovered images in Fig. 28 a_2) to e_2), high fidelity cell imaging transfer and reconstruction could be performed without any retraining for offset distance smaller than 2cm (a bending angle of ~3 degrees). The corresponding change of the normalized averaged MAE with bending is depicted in Fig. 28 f). Within this small bending limit every degree of bending results in an MAE increase of about 0.02. This is in sharp contrast to MMF-based systems which require access the distal end of the fiber to recalibrate the transmission matrix if any tiny movement (a few hundred micrometers) of the MMF happens [35, 39]. For neuroscience applications [34, 35], the flexibility of the Cell-DCNN-GALOF system shows the potential to satisfy the imaging requirements for observing real-time neuron activity in free-behaving objects.

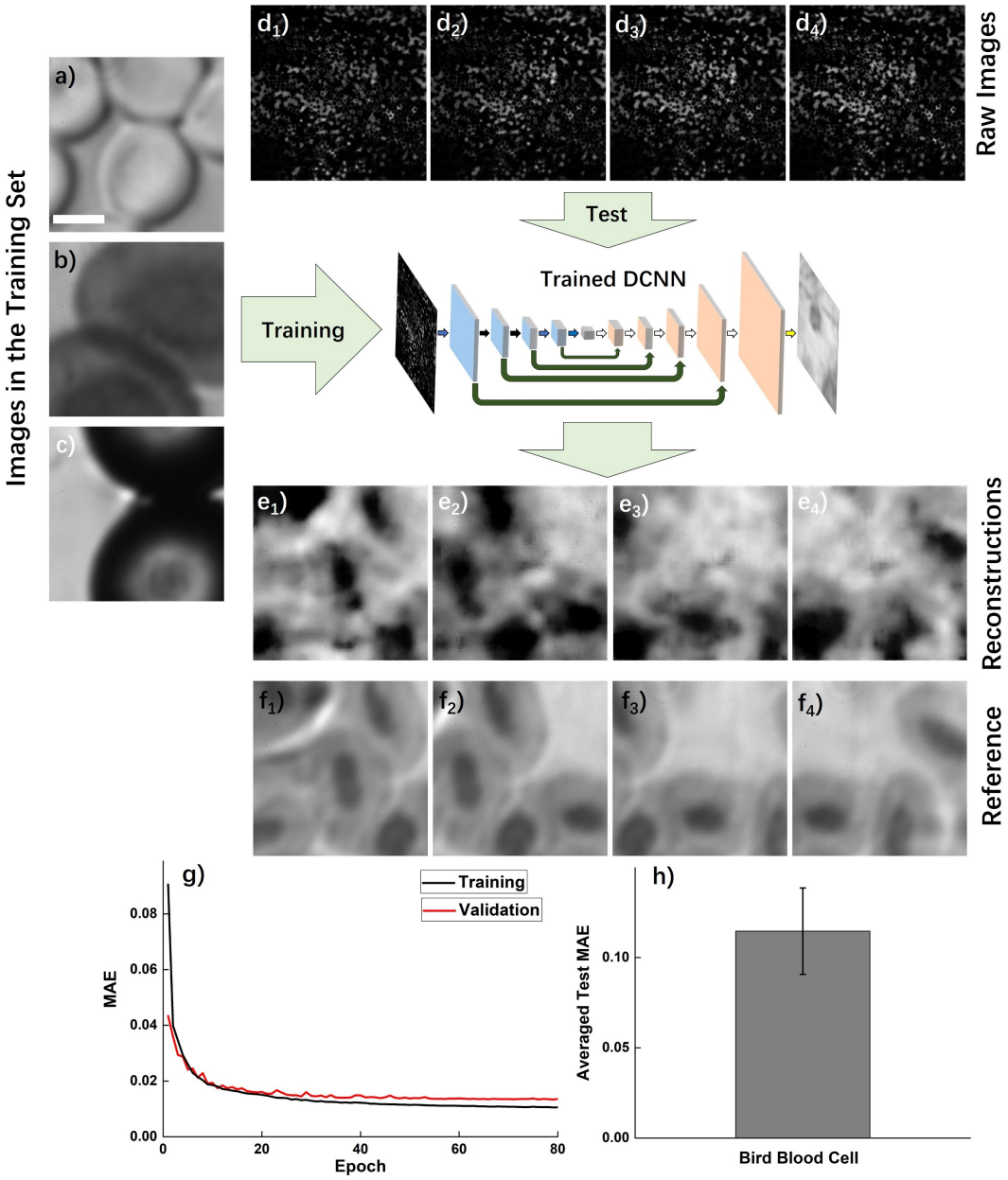

Figure 29. Cell imaging transfer learning. a)-c) are sample cell images in the set of training data. The length of the scale bar in a) is 4 μm. There are three different types of cells in the set of training data; a) is an image of human red blood cells, b) is an image of frog blood cells and c) is an image of polymer microspheres. d)-f) demonstrate the test process using data from images of bird blood cells. d_1)-d_4) are the raw images of bird blood cells transported through straight GALOF taken at 0 mm imaging depth and at room temperature. e_1)-e_4) are images reconstructed from d_1)-d_4). f_1)-f_4) are the corresponding reference images of bird blood cells. g) The training and validation accuracy improvement curves using MAE as the metric over 80 epochs. h) shows the averaged test MAE of the bird blood cells images with the standard deviation as the error bar

We have shown that our C-DCNN is able to perform high-fidelity image restoration when training and testing are performed with the same types of cells. In practical applications, the Cell-DCNN-GALOF system would be a more efficient and higher functionalized tool if it was able to transfer its learning capability to reconstruct different types of cells which never appeared in the set of training data. To enable transfer-learning reconstruction with high fidelity, a training dataset with high diversity would certainly be beneficial. As a proof-of-concept experiment, we apply a training set with just three different types of images. Sample images are shown in Fig. 29 a)-c). These are images of human red blood cells, frog blood cells, and polymer microspheres. During the recording of data for training, validation, and testing we keep the GALOF straight, the imaging plane at 0 mm depth, and at room temperature. To generate data sets for training and validation, we first collect 10000 image pairs of each human red blood cells, frog blood cells, and polymer microspheres. Subsequently, all 30000 image pairs of three different types are mixed randomly. We extract 28000 image pairs from those randomly mixed images as the training dataset and 1000 image pairs as the validation dataset. To characterize the training process, the accuracy improvement curves during training and validation are tracked and shown in Fig. 29 g). Both curves show convergence to low values after about 20 epochs. The differences between the validation and the training accuracy improvement curves are very small. These characteristics indicate that our C-DCNN is not overfitting with respect to the training dataset.

As the test data, we record 1000 image pairs from a totally different type of cells, namely bird blood cells. The raw images of the bird blood cells obtained after passing through straight GALOF are shown in Fig. 29 d). These data are fed into the trained DCNN to perform the transfer-learning reconstruction. The reconstructed and reference images are shown in Fig. 29 e) and f), respectively.

To enable a quantitative analysis, the averaged test MAE and its standard deviation are provided in Fig. 29 h). A visual inspection demonstrates that within the reconstructed images of bird blood cells one can clearly locate the position and orientation of the nucleus for every single cell. Being trained by a fairly limited set of training data, our DCNN is still able to approximately reconstruct complex cell objects of a totally different type. This transfer-learning capability Cell-DCNN-GALOF system demonstrates that the underlying physics of the imaging process is captured well by the trained C-DCNN and should prove beneficial for practical applications. At a minimum, it can be applied to cell counting tasks in biology and medicine.

The system performance of FOISs is mainly decided by the imaging processing method and the physical properties of the optical fiber. Recent developed FOISs using MMFs and MCFs heavily relies on the TM measurement and wavefront shaping which work through phase-shift interferometry and adaptive optics, such as SLM or DMD [35, 38, 47, 52]. Several shortcomings are raised by this approach [50, 53, 55]. First, incoherent light cannot be utilized in these systems. Second, the interferometric system for TM measurement makes a sophisticated experimental procedure, complicated and unstable noisy system. Third, the slow refresh rate of the expensive wavefront-shaping device (SLM or DMD) limits the imaging speed (<10Hz for most systems) and increase the cost (~30k $). Some other wavefront-shaping method using optimization algorithm without measuring TM is even slower and hard to achieve real-time imaging [48]. Besides the imaging processing method, both MMFs and MCFs are faced with several challenges in these state-of-the-art systems. Although the underlying mechanism is different, both MMFs and MCFs are unable to handle the imaging process under broadband illumination and very sensitive to perturbations [35, 38, 44, 48]. For instance, a shift of a few hundred micrometers or temperature

variation of about 15°C can mess up the MMF imaging process [35]. Although some insightful complex theoretical framework is developed recently for MMFs to predict the TM for fiber under straight or bent state, this framework is hard to be put into practical FOISs due to following reasons [75]. It not only requires precise modeling of the fiber systems but also needs customized model corrections to compensate for tiny parametric variations for a specific type of fiber. Thus, precise knowledge of the fiber's parameters, such as fiber length, refractive index distribution or bending shape, has to be known while this is extremely difficult for practical FOISs. In addition, this method still works with SLM which brings in similar problems as other wavefront-shaping methods. Another problem of MMFs and MCFs is the low mode density. For a wavelength of ~600nm mode densities are about 1 mode per μm^2 and 0.1 μm^2 for MMFs and MCFs, respectively. Especially, the diameter of the MCF has to be increased to ~ 1 millimeter in order to have enough pixels. Due to step-index guiding mechanism, expensive doped materials are required for both MMFs and MCFs. The cost is even much higher for MCFs due to the large number of individual fiber cores and a complicated fabrication process [45]. Finally, the imaging quality demonstrated by these FOISs is impaired by evident artifacts, such as noisy background, ghost images and pixelations [35, 46, 49, 52]. Some of these latest systems just show their imaging performance using binary simple objects, such as number or letters, which cannot convince their imaging ability for grayscale complex biological objects [15, 49, 64].

The Cell-DCNN-GLAOF system overcomes abovementioned disadvantages inherent in these FOISs on the basis of C-DCNN and GALOF. Regarding the imaging processing technique, the C-DCNN does not impose restrictions on coherence, bandwidth, and polarization of the light. Training and test data from intensity images are taken directly from regular CCD cameras without

any wavefront shaping device or interferometric process. On the other hand, novel properties of the GALOF lay the physics foundation for high-quality imaging. In 2018, Schirmacher *et al.* confirm that localization lengths of modes in transverse Anderson localizing fiber almost do not change within a very broad bandwidth of ~500nm [28]. This means broadband illumination does not impair the point spread function of the GALOF [28] while it is not true for MMFs and MCFs. Furthermore, unlike the MCFs the point spread function of the GALOF does not degrade with the beam propagation distance which promises high-imaging quality [25]. Besides that, the mode density of the GALOF is much higher than MMFs and MCFs, for example, 16 modes per μm^2 at ~600nm. Meanwhile, our latest research on the GALOF proves that most localized modes have nearly diffraction-limited wavefront and high spatial coherence [27]. Beyond that, the single-mode-like characteristics of localized modes maximize the robustness of the imaging process [26, 27]. All these superior properties are based on a low-cost GALOF: non-doped cheap silica and simple two-step stack-and-draw fabrication [15]. On the combination of C-DCNN and GALOF, the system performance makes a big leap forward. High speed (~20 Hz) artifact-free biological cell imaging is realized under broadband incoherent illumination based on a very simple, stable and cheap system. In particular, the imaging speed is just decided by cheap hardware of a personal computer. For the same setup in this paper, an even faster speed can be easily achieved if using better GPUs (~2k $). Also, the tolerance of 3 degrees bending and 30 °C thermal change stand for significant progress compared to other state-of-the-art systems. In addition to the above advantages, lensless imaging and transfer-learning capability are another two important progress compared to previous systems. For lensless imaging, the Cell-DCNN-GALOF can still maintain high-quality imaging for biological objects that are several millimeters away (<4mm). Some other FOISs which

demonstrate lensless imaging just show low imaging quality with a much smaller imaging depth (a few hundred micrometers) [35, 49]. Regarding the transfer-learning performance, previous deep-learning-based FOISs just demonstrate quite limited capabilities in that the morphology of test objects are quite similar to training objects (simple binary numbers or letters) [15, 64]. Our imaging system has shown more powerful and practical transfer-learning capabilities through reconstructing cell objects that are not part of any training procedure.

As a proof-of-concept system, there is still lots of room for improvement in the future. First of all, the current setup works under transmission mode while reflection operation mode is more suitable for practical i*n vivo* imaging. As demonstrated by Mafi's group, a part of GALOF's random structure can be used to guide illumination light that is coupled from the proximal end, and the other parts can be applied to transport the image back from the distal end [27, 76]. Thus, it is straightforward to switch to a reflection-mode system. Second, even if the lensless imaging depth of the Cell-DCNN-GALOF system is able to satisfy lots of practical applications, it is always desired to extend the imaging depth further. The imaging quality of the current system gradually reduces with increasing the depth. This might be attributed to the fact that, under incoherent illumination, high-frequency features of the intensity objects are gradually lost with increasing imaging depth leading to a corresponding rise of the MAE. In future work, this problem might be relieved through optimizing structural parameters of the GALOF. Third, it is worth noting that the imaging quality of the Cell-DCNN-GALOF system starts to degrade if the bending is larger than 3 degrees. This might be attributed to remaining extended modes embedded in the random structure even if most transmission channels demonstrate single-mode properties [27]. The path to improved bending independence will be further optimization of the random structure inside the

GALOF. It should be possible to maximize the scattering in the transverse plane to further enhance light localization by using new materials and tuning air-filling fraction. Enhanced Anderson localization creates localization lengths with smaller radii and less variations [21, 23, 27]. Therefore, GALOF-based imaging system could potentially provide even stronger robustness through optimization of GALOF design and fabrication. Finally, a lot of improvements in transfer-learning imaging can be achieved when suitable training data with larger diversity are applied. However, generating highly diverse biological training data for a FOIS remains a formidable practical challenge and the computational power available to process large amounts of training data is often an additional bottleneck. We believe that these challenges can be addressed in next generation FIOSs for biological objects with the help of further optimized C-DCNN architectures.

In conclusion, it is the combination of unique GALOF properties and tailored C-DCNN design that enables the remarkable capabilities of the presented Cell-DCNN-GALOF imaging system. Both components, GALOF design and C-DCNN architecture, still have room for improvements and future research will consider both components and their interplay. We are very optimistic that the presented architecture can be the bases for future high-fidelity imaging systems that are minimally invasive and feature robust performance in dynamic environments

APPENDIX: PUBLICATIONS

Journal Publications:

J. Zhao, Y. Sun, H. Zhu, Z. Zhu, J. E. Antonio-Lopez, R. A. Correa, S. Pang, and A. Schülzgen, “Deep Learning Cell Imaging through Anderson Localizing Optical Fibre,” Nature Communications, Manuscript ID: NCOMMS-18-34827, under consideration.

J. Zhao, M. Peysokhan, J. E. Antonio-Lopez, Y. Sun, B. Abaie, A. Mafi, R. Amezcua Correa, S. Pang, and A. Schülzgen, "A path to high-quality imaging through disordered optical fibers: a review," Appl. Opt. **58**, D50-D60 (2019).

J. Zhao, Y. Sun, Z. Zhu, J. E. Antonio-Lopez, R. A. Correa, S. Pang, and A. Schülzgen, "Deep Learning Imaging through Fully-Flexible Glass-Air Disordered Fiber," ACS Photonics **5**, 3930-3935 (2018).

J. Zhao, J. E. A. Lopez, Z. Zhu, D. Zheng, S. Pang, R. A. Correa, and A. Schülzgen, "Image Transport Through Meter-Long Randomly Disordered Silica-Air Optical Fiber," Scientific Reports **8**, 3065 (2018).

S. Fan, S. Smith-Dryden, **J. Zhao**, S. Gausmann, A. Schülzgen, G. Li, and B. E. A. Saleh, "Optical Fiber Refractive Index Profiling by Iterative Optical Diffraction Tomography," Journal of Lightwave Technology **36**, 5754-5763 (2018).

B. Abaie, M. Peysokhan, **J. Zhao**, J. E. Antonio-Lopez, R. Amezcua-Correa, A. Schülzgen, and A. Mafi, "Disorder-induced high-quality wavefront in an Anderson localizing optical fiber," Optica **5**, 984-987 (2018).

Y. Wang, T. Guo, J. Li, **J. Zhao**, Y. Yin, X. Ren, J. Li, Y. Wu, M. Weidman, Z. Chang, M. F. Jager, C. J. Kaplan, R. Geneaux, C. Ott, D. M. Neumark, and S. R. Leone, "Enhanced high-order harmonic generation driven by a wavefront corrected high-energy laser," Journal of Physics B: Atomic, Molecular and Optical Physics **51**, 134005 (2018).

D. Zheng, L. Chen, J. Li, Q. Sun, W. Zhu, J. Anderson, **J. Zhao**, and A. Schülzgen, "Circular carrier squeezing interferometry: Suppressing phase shift error in simultaneous phase-shifting point-diffraction interferometer," Optics and Lasers in Engineering **102**, 136-142 (2018).

Conference Proceedings

J. Zhao, Y. Sun, J. E. Antonio-Lopez, R. A. Correa, S. Pang, A. Schülzgen, “Cell Imaging Using Glass-Air Disordered Optical Fiber and Deep Learning Algorithms,” *Imaging and Applied Optics 2019*, accepted.

J. Zhao, Y. Sun, J. E. Antonio-Lopez, R. A. Correa, S. Pang, and A. Schülzgen, “Robust Cell Imaging through Anderson Localizing Optical Fiber Based on Deep Learning,” *Conference on Lasers and Electro-Optics (CLEO) 2019*, accepted.

B. Abaie, M. Peysokhan, **J. Zhao**, J. E. Antonio-Lopez, R. Amezcua-Correa, A. Schülzgen, and A. Mafi, *Enhancement of wavefront characteristics in fibers by Anderson localized modes (Conference Presentation)*, SPIE OPTO (SPIE, 2019), Vol. 10935.

J. Zhao, Y. Sun, Z. Zhu, J. E. Antonio-Lopez, R. A. Correa, S. Pang, and A. Schülzgen, "Randomly Disordered Glass-Air Optical Fiber Imaging Based on Deep Learning," in *Advanced Photonics 2018 (BGPP, IPR, NP, NOMA, Sensors, Networks, SPPCom, SOF)*, OSA Technical Digest (online) (Optical Society of America, 2018), SoW1H.2.

J. Zhao, Y. Sun, Z. Zhu, D. Zheng, J. E. Antonio-Lopez, R. A. Correa, S. Pang, and A. Schülzgen, "Bending-Independent Imaging through Glass-Air Disordered Fiber Based on Deep Learning," in *Imaging and Applied Optics 2018 (3D, AO, AIO, COSI, DH, IS, LACSEA, LS&C, MATH, pcAOP)*, OSA Technical Digest (Optical Society of America, 2018), CW3B.6.

J. Zhao, Y. Sun, Z. Zhu, D. Zheng, J. E. Antonio-Lopez, R. A. Correa, S. Pang, and A. Schülzgen, "Deep-Learning-Based Imaging through Glass-Air Disordered Fiber with Transverse Anderson Localization," in *Conference on Lasers and Electro-Optics*, OSA Technical Digest (online) (Optical Society of America, 2018), STu3K.3.

B. Abaie, M. Peysokhan, **J. Zhao**, J. E. Antonio-Lopez, R. Amezcua-Correa, A. Schlzgen, and A. Mafi, "Nearly diffraction limited beam qualities in an Anderson localizing optical fiber," in *Conference on Lasers and Electro-Optics*, OSA Technical Digest (online) (Optical Society of America, 2018), STu3K.2.

J. E. Antonio-Lopez, **J. Zhao**, J. C. Alvarado-Zacarias, J. Villatoro, A. Schülzgen, and R. A. Correa, "Dual-core fiber interferometer for sensing applications," *Fifth Workshop on Specialty Optical Fibers and Their Applications — WSOF 2017*, Proc. of SPIE Vol. 10604 1060401-176.

J. Zhao, J. E. Antonio-Lopez, R. A. Correa, D. Zheng, and A. Schülzgen, "Image Transport Through Meter-Long Silica-Air Disordered Optical Fiber," *Fifth Workshop on Specialty Optical Fibers and Their Applications — WSOF 2017*, Proc. of SPIE Vol. 10604 1060401-28 (**Invited**).

J. Zhao, J. E. Antonio-Lopez, R. A. Correa, A. Mafi, M. Windeck, and A. Schülzgen, "Image Transport Through Silica-Air Random Core Optical Fiber," in *Conference on Lasers and Electro-Optics*, OSA Technical Digest (online) (Optical Society of America, 2017), JTu5A.91.

V. O. Smolski, S. D. Gorelov, **J. Zhao**, J. Xu, P. G. Schunemann, and K. L. Vodopyanov, "Frequency Comb Spanning 2.5-7.5 μm from a Subharmonic GaAs OPO and its Coherence Properties," in *CLEO: 2015*, OSA Technical Digest (online) (Optical Society of America, 2015), STh1N.5.

LIST OF REFERENCES

1. Anderson, P.W., *Absence of Diffusion in Certain Random Lattices.* Physical Review, 1958. **109**(5): p. 1492-1505.
2. John, S., *Localization of Light.* Physics Today, 1991. **44**(5): p. 32.
3. Graham, I.S., L. Piché, and M. Grant, *Experimental evidence for localization of acoustic waves in three dimensions.* Physical Review Letters, 1990. **64**(26): p. 3135-3138.
4. Hu, H., et al., *Localization of ultrasound in a three-dimensional elastic network.* Nature Physics, 2008. **4**: p. 945.
5. Chabanov, A.A., M. Stoytchev, and A.Z. Genack, *Statistical signatures of photon localization.* Nature, 2000. **404**(6780): p. 850-853.
6. Cao, H., et al., *Random Laser Action in Semiconductor Powder.* Physical Review Letters, 1999. **82**(11): p. 2278-2281.
7. Karbasi, S., et al., *Image transport through a disordered optical fibre mediated by transverse Anderson localization.* Nat Commun, 2014. **5**.
8. Abaie, B., et al., *Random lasing in an Anderson localizing optical fiber.* Light Sci Appl., 2017. **6**: p. e17041.
9. Crane, T., et al., *Anderson Localization of Visible Light on a Nanophotonic Chip.* ACS Photonics, 2017. **4**(9): p. 2274-2280.
10. Trojak, O.J., T. Crane, and L. Sapienza, *Optical sensing with Anderson-localised light.* Applied Physics Letters, 2017. **111**(14): p. 141103.
11. Choi, S.H., et al., *Anderson light localization in biological nanostructures of native silk.* Nature Communications, 2018. **9**(1): p. 452.

12. Zhao, J., et al., *Image Transport Through Meter-Long Randomly Disordered Silica-Air Optical Fiber.* Scientific Reports, 2018. **8**(1): p. 3065.

13. Tuan, T.H., et al., *Near-infrared optical image transport through an all-solid tellurite optical glass rod with transversely-disordered refractive index profile.* Optics Express, 2018. **26**(13): p. 16054-16062.

14. Shi, N.N., et al., *Nanostructured fibers as a versatile photonic platform: radiative cooling and waveguiding through transverse Anderson localization.* Light: Science & Applications, 2018. **7**(1): p. 37.

15. Zhao, J., et al., *Deep Learning Imaging through Fully-Flexible Glass-Air Disordered Fiber.* ACS Photonics, 2018. **5**(10): p. 3930-3935.

16. Ioffe, A.F. and A.R. Regel, *Non-crystalline, amorphous and liquid electronic semiconductors.* Progress in Semiconductors, 1960. **4**: p. 237-291.

17. De Raedt, H., A. Lagendijk, and P. de Vries, *Transverse Localization of Light.* Physical Review Letters, 1989. **62**(1): p. 47-50.

18. Schwartz, T., et al., *Transport and Anderson localization in disordered two-dimensional photonic lattices.* Nature, 2007. **446**(7131): p. 52-55.

19. Karbasi, S., et al., *Observation of transverse Anderson localization in an optical fiber.* Optics Letters, 2012. **37**(12): p. 2304-2306.

20. Abdullaev, S.S. and F.K. Abdullaev, *On propagation of light in fiber bundles with random parameters.* Radiofizika, 1980. **23**: p. 766-767.

21. Karbasi, S., et al., *Detailed investigation of the impact of the fiber design parameters on the transverse Anderson localization of light in disordered optical fibers.* Optics Express, 2012. **20**(17): p. 18692-18706.

22. Karbasi, S., K.W. Koch, and A. Mafi, *Multiple-beam propagation in an Anderson localized optical fiber.* Optics Express, 2013. **21**(1): p. 305-313.

23. Karbasi, S., K.W. Koch, and A. Mafi, *Modal perspective on the transverse Anderson localization of light in disordered optical lattices.* Journal of the Optical Society of America B, 2013. **30**(6): p. 1452-1461.

24. Abaie, B. and A. Mafi, *Scaling analysis of transverse Anderson localization in a disordered optical waveguide.* Physical Review B, 2016. **94**(6): p. 064201.

25. Karbasi, S., K.W. Koch, and A. Mafi, *Image transport quality can be improved in disordered waveguides.* Optics Communications, 2013. **311**: p. 72-76.

26. Ruocco, G., et al., *Disorder-induced single-mode transmission.* Nat Commun, 2017. **8**: p. 14571.

27. Abaie, B., et al., *Disorder-induced high-quality wavefront in an Anderson localizing optical fiber.* Optica, 2018. **5**(8): p. 984-987.

28. Schirmacher, W., et al., *What is the Right Theory for Anderson Localization of Light? An Experimental Test.* Physical Review Letters, 2018. **120**(6): p. 067401.

29. Mafi, A., *Transverse Anderson localization of light: a tutorial.* Advances in Optics and Photonics, 2015. **7**(3): p. 459-515.

30. Karbasi, S., et al., *Transverse Anderson localization in a disordered glass optical fiber.* Optical Materials Express, 2012. **2**(11): p. 1496-1503.

31. Zhao, J., et al. *Image Transport Through Silica-Air Random Core Optical Fiber*. in *Conference on Lasers and Electro-Optics*. 2017. San Jose, California: Optical Society of America.

32. Flusberg, B.A., et al., *Fiber-optic fluorescence imaging.* Nat Methods, 2005. **2**(12): p. 941-50.

33. Liu, J.T.C., et al., *Point-of-care Pathology with Miniature Microscopes.* Analytical Cellular Pathology, 2011. **34**(3).

34. Szabo, V., et al., *Spatially Selective Holographic Photoactivation and Functional Fluorescence Imaging in Freely Behaving Mice with a Fiberscope.* Neuron, 2014. **84**(6): p. 1157-1169.

35. Ohayon, S., et al., *Minimally invasive multimode optical fiber microendoscope for deep brain fluorescence imaging.* Biomedical Optics Express, 2018. **9**(4): p. 1492-1509.

36. Yelin, D., et al., *Three-dimensional miniature endoscopy.* Nature, 2006. **443**: p. 765.

37. Abramov, A., L. Minai, and D. Yelin, *Multiple-channel spectrally encoded imaging.* Optics Express, 2010. **18**(14): p. 14745-14751.

38. Cizmar, T. and K. Dholakia, *Exploiting multimode waveguides for pure fibre-based imaging.* Nat Commun, 2012. **3**: p. 1027.

39. Choi, Y., et al., *Scanner-Free and Wide-Field Endoscopic Imaging by Using a Single Multimode Optical Fiber.* Physical Review Letters, 2012. **109**(20): p. 203901.

40. Papadopoulos, I.N., et al., *High-resolution, lensless endoscope based on digital scanning through a multimode optical fiber.* Biomedical Optics Express, 2013. **4**(2): p. 260-270.

41. Hughes, M., T.P. Chang, and G.-Z. Yang, *Fiber bundle endocytoscopy.* Biomedical Optics Express, 2013. **4**(12): p. 2781-2794.

42. Ducourthial, G., et al., *Development of a real-time flexible multiphoton microendoscope for label-free imaging in a live animal.* Scientific Reports, 2015. **5**: p. 18303.

43. Reichenbach, K.L. and C. Xu, *Numerical analysis of light propagation in image fibers or coherent fiber bundles.* Optics Express, 2007. **15**(5): p. 2151-2165.

44. Chen, X., K.L. Reichenbach, and C. Xu, *Experimental and theoretical analysis of core-to-core coupling on fiber bundle imaging.* Optics Express, 2008. **16**(26): p. 21598-21607.

45. Stone, J.M., et al., *Low index contrast imaging fibers.* Optics Letters, 2017. **42**(8): p. 1484-1487.

46. Chang, Y., et al., *Compact high-resolution endomicroscopy based on fiber bundles and image stitching.* Optics Letters, 2018. **43**(17): p. 4168-4171.

47. Kim, D., et al., *Toward a miniature endomicroscope: pixelation-free and diffraction-limited imaging through a fiber bundle.* Optics Letters, 2014. **39**(7): p. 1921-1924.

48. Weiss, U. and O. Katz, *Two-photon lensless micro-endoscopy with in-situ wavefront correction.* Optics Express, 2018. **26**(22): p. 28808-28817.

49. Tsvirkun, V., et al., *Widefield lensless endoscopy with a multicore fiber.* Optics Letters, 2016. **41**(20): p. 4771-4774.

50. Andresen, E.R., et al., *Ultrathin endoscopes based on multicore fibers and adaptive optics: a status review and perspectives*. Vol. 21. 2016: SPIE. 12.

51. Čižmár, T. and K. Dholakia, *Shaping the light transmission through a multimode optical fibre: complex transformation analysis and applications in biophotonics.* Optics Express, 2011. **19**(20): p. 18871-18884.

52. Turtaev, S., et al., *High-fidelity multimode fibre-based endoscopy for deep brain in vivo imaging.* Light: Science & Applications, 2018. **7**(1): p. 92.

53. Popoff, S.M., et al., *Controlling light through optical disordered media: transmission matrix approach.* New Journal of Physics, 2011. **13**(12): p. 123021.

54. Popoff, S.M., et al., *Measuring the Transmission Matrix in Optics: An Approach to the Study and Control of Light Propagation in Disordered Media.* Physical Review Letters, 2010. **104**(10): p. 100601.

55. Yu, H., et al., *Recent advances in wavefront shaping techniques for biomedical applications.* Current Applied Physics, 2015. **15**(5): p. 632-641.

56. Forbes, A., A. Dudley, and M. McLaren, *Creation and detection of optical modes with spatial light modulators.* Advances in Optics and Photonics, 2016. **8**(2): p. 200-227.

57. LeCun, Y., Y. Bengio, and G. Hinton, *Deep learning.* Nature, 2015. **521**(7553): p. 436-44.

58. Dong, C., et al., *Image Super-Resolution Using Deep Convolutional Networks.* IEEE Trans Pattern Anal Mach Intell, 2016. **38**(2): p. 295-307.

59. Sinha, A., et al., *Lensless computational imaging through deep learning.* Optica, 2017. **4**(9): p. 1117-1125.

60. Rivenson, Y., et al., *Deep learning microscopy.* Optica, 2017. **4**(11): p. 1437-1443.

61. Li, S., et al., *Imaging through glass diffusers using densely connected convolutional networks.* Optica, 2018. **5**(7): p. 803-813.

62. Nguyen, T., et al., *Deep learning approach for Fourier ptychography microscopy.* Optics Express, 2018. **26**(20): p. 26470-26484.

63. Borhani, N., et al., *Learning to see through multimode fibers.* Optica, 2018. **5**(8): p. 960-966.

64. Rahmani, B., et al., *Multimode optical fiber transmission with a deep learning network.* Light: Science & Applications, 2018. **7**(1): p. 69.

65. Li, Y., Y. Xue, and L. Tian, *Deep speckle correlation: a deep learning approach toward scalable imaging through scattering media.* Optica, 2018. **5**(10): p. 1181-1190.

66. Sun, Y., X. Yuan, and S. Pang, *High-speed compressive range imaging based on active illumination.* Optics Express, 2016. **24**(20): p. 22836-22846.

67. Sun, Y., X. Yuan, and S. Pang, *Compressive high-speed stereo imaging.* Optics Express, 2017. **25**(15): p. 18182-18190.

68. Mao, X.-J., C. Shen, and Y.-B. Yang, *Image Restoration Using Convolutional Auto-encoders with Symmetric Skip Connections.* arXiv:1606.08921, 2016.

69. Kingma, D.P. and J. Ba, *Adam: A Method for Stochastic Optimization.* arXiv:1412.6980, 2014.

70. Leonetti, M., et al., *Experimental observation of disorder induced self-focusing in optical fibers.* Applied Physics Letters, 2014. **105**(17): p. 171102.

71. Wang, Z. and A.C. Bovik, *Mean squared error: Love it or leave it? A new look at Signal Fidelity Measures.* IEEE Signal Processing Magazine, 2009. **26**(1): p. 98-117.

72. Zhou, W., et al., *Image quality assessment: from error visibility to structural similarity.* IEEE Transactions on Image Processing, 2004. **13**(4): p. 600-612.

73. Wood, H.A.C., et al., *High-resolution air-clad imaging fibers.* Optics Letters, 2018. **43**(21): p. 5311-5314.

74. Albeanu, D.F., et al., *LED Arrays as Cost Effective and Efficient Light Sources for Widefield Microscopy.* PLOS ONE, 2008. **3**(5): p. e2146.

75. Plöschner, M., T. Tyc, and T. Čižmár, *Seeing through chaos in multimode fibres.* Nat Photon, 2015. **9**(8): p. 529-535.

76. Mafi, A., et al., *Disordered Anderson Localization Optical Fibers for Image Transport-A Review.* arXiv:1902.00433, 2019.